Diagnosis of physical and biological controls on phytoplankton distribution in the Gulf of Maine-Georges Bank region

by

Caixia Wang

B.S. in Applied Mathematics, Ocean University of Qingdao (1993)
M.S. in Physical Oceanography, Ocean University of Qingdao,
Qingdao, China (1996)

Submitted to the Joint Program in Physical Oceanography
in partial fulfillment of the requirements for the degree of

Master of Science

at the

MASSACHUSETTS INSTITUTE OF TECHNOLOGY

June 1999

© Caixia Wang 1999. All rights reserved.

Author ....
Joint Program in Physical Oceanography
May 7, 1999

Certified by ....
Paola Malanotte-Rizzoli
Professor
Thesis Supervisor

Accepted by ....
Brechner W. Owens
Chairman, Joint Committee for Physical Oceanography
Massachusetts Institute of Technology
Woods Hole Oceanographic Institution

20020116 174

Diagnosis of physical and biological controls on phytoplankton distribution in the Gulf of Maine-Georges Bank region

by

Caixia Wang

Submitted to the Joint Program in Physical Oceanography
on May 7, 1999, in partial fulfillment of the
requirements for the degree of
Master of Science

Abstract

The linkage between physics and biology is studied by applying a one-dimensional model and a two-dimensional model to the Sargasso Sea and the Gulf of Maine-Georges Bank region, respectively. The first model investigates the annual cycles of production and the response of the annual cycles to external forcing. The computed seasonal cycles compare reasonably well with the data. The spring bloom occurs after the winter mixing weakens and before the establishment of the summer stratification. Sensitivity experiments are also carried out, which basically provide information of how the internal bio-chemical parameters affect the biological system. The second model investigates the effect of the circulation field on the distribution of phytoplankton, and the relative importance of physical circulation and biological sources by using a data assimilation approach. The model results reveal seasonal and geographic variations of phytoplankton concentration, which compare well with data. The results verify that the seasonal cycles of phytoplankton are controlled by both the biological source and the physical advection, which themselves are functions of space and time. The biological source and the physical advection basically counterbalance each other. Advection controls the tendency of the phytoplankton concentration more often in the coastal region of the western Gulf of Maine than on Georges Bank, due to the small magnitude of the biological source in the former region, although the advection flux divergences have greater magnitudes on Georges Bank than in the coastal region of the western Gulf of Maine. It is also suggested by the model results that the two separated populations in the coastal region of the western Gulf of Maine and on Georges Bank are self-sustaining.

Thesis Supervisor: Paola Malanotte-Rizzoli
Title: Professor

Contents

List of Figures

7

List of Tables

Chapter 1

Introduction

Photosynthesis, the conversion of solar energy to chemical energy, is a fundamental step by which inorganic carbon is fixed by algae and converted into primary production. Significant rates of primary production can occur only in the well-lit euphotic zone. Hence, the animals which feed on the primary production can survive mostly within the mixed layer where there are high levels of food for them. Physical processes play an important role in marine ecosystem dynamics (Mann and Lazier, 1991) and can modify or limit biological production through the nutrients supply and mean irradiance field (e.g. McClain et al., 1990; Mitchell et al., 1991). This thesis studies the linkage between physics and biology via the application of two physical-biological coupled models. The first model is one-dimensional, designed to investigate the vertical structure of a simple biochemical model coupled to a physical model of the upper ocean mixed layer, with an application to the Sargasso Sea. The second model is a two-dimensional advection-diffusion-reaction equation for biology concentration, with a source or sink term determined through an assimilation approach. The model is designed to investigate the effect of the horizontal circulation on the biology distribution and is applied to the Gulf of Maine-Georges Bank region.

The depth of the mixed layer, the intensity of the solar radiation penetrating into the water column and the distribution of the dissolved nutrients with depth are some of the major factors regulating the biosystem of the sea. The seasonal variation in the atmosphere-ocean heat flux imparts a seasonal cycle to the depth of the mixed layer (Sverdrup et al., 1942; Menzel and Ryther, 1960). The variation of wind stress also affects the depth of the mixed layer. According to Menzel and Ryther (1960), production in the Sargasso Sea off Bermuda is closely dependent upon vertical mixing, high levels occurring when the water is isothermal and mixed to or near the depth of the permanent thermocline (400 m), low levels being associated with the presence of a seasonal thermocline in the upper 100 m.

The goal of Chapter 2 is to investigate and understand the interplaying and relative importance of the physical vertical processes occurring in the euphotic zone in determining the vertical distribution of nutrients and biology. The biochemical part comprises five components, i.e. nitrate, ammonium, phytoplankton, zooplankton and detritus (Oguz et al., 1996). A case-study is carried out by applying the model to the Sargasso Sea oligotrophic region, using the U. S. Joint Global Ocean Flux Study (JGOFS) Bermuda Atlantic Time-series Study (BATS) site data. The coupling between the biological and physical model is accomplished by vertical mixing coefficients. In this chapter, we first study the seasonal response of the mixed layer physics and biology to the external forcing (wind-stress, heat flux, and surface salinity). Successively we perform a sensitivity analysis of the model components to the biochemical parameters. The details of the impact of nutrients, light availability, and the interaction between the biochemicals and production are examined through the sensitivity experiments. Ecosystem models have now widespread applications for different oceanic conditions (e.g., Varela et al., 1992; Radach and Moll, 1993; Sharples and Tett, 1994). Another more recent application of a similar coupled physical-biological model to the BATS data (Doney et al., 1996) was very successful

in reproducing the seasonal cycles of the upper water column temperature field, as well as of the chlorophyll and primary production.

The focus of Chapter 2 is on the vertical physical and biochemical processes. However, the horizontal flow field does affect the biological system (e.g. Campbell, 1986; Campbell and Wroblewski, 1985; Flierl and Davis, 1993; Franks and Chen, 1996; McGillicuddy et al., 1998). Therefore, the goal of Chapter 3 and 4 is to investigate and understand how advection and diffusion processes determined by the horizontal circulation affect the horizontal distribution of phytoplankton with relationship to growth versus mortality region. An application is carried out for the Gulf of Maine-Georges Bank region.

Georges Bank is one of the most productive shelf ecosystems in the world (O'Reilly et al., 1987; Cohen and Grosslein, 1987), having an annual area-weighted production two-to-three times that of the world's average for continental shelves. Interdisciplinary field programs examining the physics and biology of the region have shown the high rates of production to be strongly linked to the unusual circulation dynamics on the Bank (e.g., Riley, 1941; Cohen et al., 1982; Horne et al., 1989). A two-dimensional (x, z) coupled physical-biological model of the plankton on Georges Bank during the summer was developed by Franks and Chen in 1996. In their study, the physically forced vertically integrated fluxes of phytoplankton, zooplankton, and nutrients on and off the Bank were quantified, with the biological variables behaving as conservative, passive tracers. Their study showed that the largest changes occurred within the fronts, where biochemicals were transported from deep waters toward the shallow waters of the Bank. The phytoplankton field became vertically homogeneous on the top of the Bank, with slightly decreasing concentrations from south to north. A patch of high phytoplankton biomass formed in the northern tidal front.

The geomorphological, physical, chemical, and biological characteristics of the Gulf of Maine are reasonably consistent with the current concept of an estuary

(Campbell, 1986). A prominent characteristic of estuaries is that the import and export of materials and organisms play important roles in controlling biological production within the system (Margalef, 1967). Riley (1967 a) modeled the effects of shoreward nutrient transport on the productivity of coastal waters off southern New England. He concluded that nutrient transport was an important factor explaining the distribution of biological productivity across the continental shelf.

In the Gulf of Maine-Georges Bank region, McGillicuddy et al. (1998) utilized an adjoint data assimilation method to determine the mechanisms that control seasonal variations in the abundance of Pseudocalanus spp. It was postulated in his model that the observed distributions result from the interaction of the population dynamics with the climatological circulation. The problem was posed mathematically as a 2-D (x, y) advection-diffusion-reaction equation for a scalar variable.

The second part of this thesis applies the above model of McGillicuddy et al. (1998) to the Gulf of Maine-Georges Bank region, with the Chlorophyll a data from the Marine Resources Monitoring, Assessment and Prediction program (MARMAP) of the National Oceanographic and Atmospheric Administration, Northeast Fisheries Science Center between 1977 and 1988 (O'Reilly and Zetlin, 1996). In Chapter 3, the OAX - optimal linear estimation package is used to map and analyse the observation of phytoplankton Chlorophyll a in the Gulf of Maine-Georges region. Experiments are also carried out to test the sensitivity of the mapping results to the model parameters. Chapter 4 focuses on the adjoint data assimilation approach and the analysis of the model results. The investigation is separated into six bi-monthly periods and confined to the "region of interest", as defined in McGillicuddy et al., 1998, a region not affected by boundary conditions and where data are available.

The future of this study lies in the combination of the above two types of models, i.e. a full three-dimensional approach that allows to access the relative importance of vertical versus horizontal processes in the dynamics of the ecosystem.

Chapter 2

Applications of a one-dimensional physical-biological model to Sargasso Sea

2.1 The model

The complete model includes the physical and biological submodels. The model is restricted to two dimensions (time and depth), in which the vertical mixing process is parameterized by the level 2.5 Mellor and Yamada (1982) turbulence closure scheme. It involves a fairly sophisticated mixed layer dynamics. Its biology is kept intentionally simple to understand and explore the basic biological interactions and mechanisms.

2.1.1 The physical model

The physical model is the one-dimemsional version of the Princeton Ocean Model (Blumberg and Mellor, 1987). For a horizontally homogeneous, incompressible, Boussinesq and hydrostatic sea without any vertical water motion, the horizontal momentum

equation is expressed as

$$\frac{\partial \vec{u}}{\partial t} - f\hat{k} \times \vec{u} = \frac{\partial}{\partial z}\left[(K_m + \nu_m)(\frac{\partial \vec{u}}{\partial z})\right] \tag{2.1.1}$$

where t is time, z is the vertical coordinate, $\vec{u}$ is the horizontal velocity of the mean flow with the components (u, v), $\hat{k}$ is the unit vector in the vertical direction, and f is the Coriolis parameter. K_m denotes the coefficient for the vertical turbulent diffusion of momentum, and ν_m represents its background value associated with internal wave mixing and other small-scale mixing processes.

The temperature T and salinity S are determined from transport equations of the form

$$\frac{\partial C}{\partial t} = \frac{\partial}{\partial z}\left[(K_h + \nu_h)(\frac{\partial C}{\partial z})\right] \tag{2.1.2}$$

where C denotes either T or S, K_h is the coefficient for the vertical turbulent heat and salt diffusions, and ν_h is its background value. For simplicity, the solar irradiance which penetrates into the water column is not parameterized separately in the temperature equation. It is respresented through the surface boundary condition given in (1.2.4) together with other components of the total heat flux. The density is functions of the potential temperature, salinity and pressure, $\rho = \rho(T, S, p)$ using a non-linear equation of state (Mellor, 1990).

The vertical mixing coefficients are determined from

$$(K_m, K_h) = lq(S_m, S_h) \tag{2.1.3}$$

where l and q are the turbulent length scale and turbulent velocity, respectively. S_m and S_h are the stability factors expressed by Mellor and Yamada (1982). In the level 2.5 turbulence closure, l and q are computed from the turbulent kinetic

14

energy, $\frac{1}{2}q^2$, and the turbulent macroscale equations. The turbulent buoyancy and shear productions are calculated by the vertical shear of the horizontal velocity and the vertical density gradient of the mean flow. K_h is assumed to represent the eddy coefficient for vertical turbulent diffusion of the biological variable as well.

The boundary conditions at the sea surface z=0 are

$$\rho_0 K_m \frac{\partial \vec{u}}{\partial z} = \vec{\tau}_s \qquad (2.1.4)$$

$$K_h \frac{\partial T}{\partial z} = \frac{Q_H}{\rho_0 c_p} \qquad (2.1.5)$$

$$S = S_0 \qquad (2.1.6)$$

where $\vec{\tau}_s$ is the wind stress vector at the sea surface, Q_H is the net sea surface heat flux, S_0 is the sea surface salinity, ρ_0 is the reference density and c_p is the specific heat of water. The bottom of the model is taken at 400 meter. No stress, no-heat and no-salt flux conditions are specified at the bottom

$$\rho_0 K_m \frac{\partial \vec{u}}{\partial z} = 0 \qquad (2.1.7)$$

$$K_h \frac{\partial C}{\partial z} = 0 \qquad (2.1.8)$$

where C again denotes either T or S.

2.1.2 The biological model

Biological constituents in the coupled model are treated as equivalent scalar concentrations of nitrogen ($mmol N m^{-3}$). Nitrogen plays a critical role in ocean biology as

an important limiting nutrient, particularly in subtropical gyres, and is a natural currency for studying biological flows (Fasham et al., 1990). The biological scalars advect and diffuse following the physical rules outlined above and the biological interactions are modeled as flows of nitrogen between compartments. The art in ecosystem modelling lies in identifying the appropriate types of compartments and their linkages. Detailed models may lead to better, more realistic simulations, but at the expense of added complexity, less interpratable solutions and increasing number of free parameters that must be specified and for which we have few reliable estimates. Therefore, in our model , an attempt has been made to keep the model as simple as possible without eliminating essential dynamics of the system. The simple, five-component system - phytoplankton (P), zooplankton (Z), nitrate (N), ammonium (A) and detritus (D) is outlined schematically in Figure 2-1.
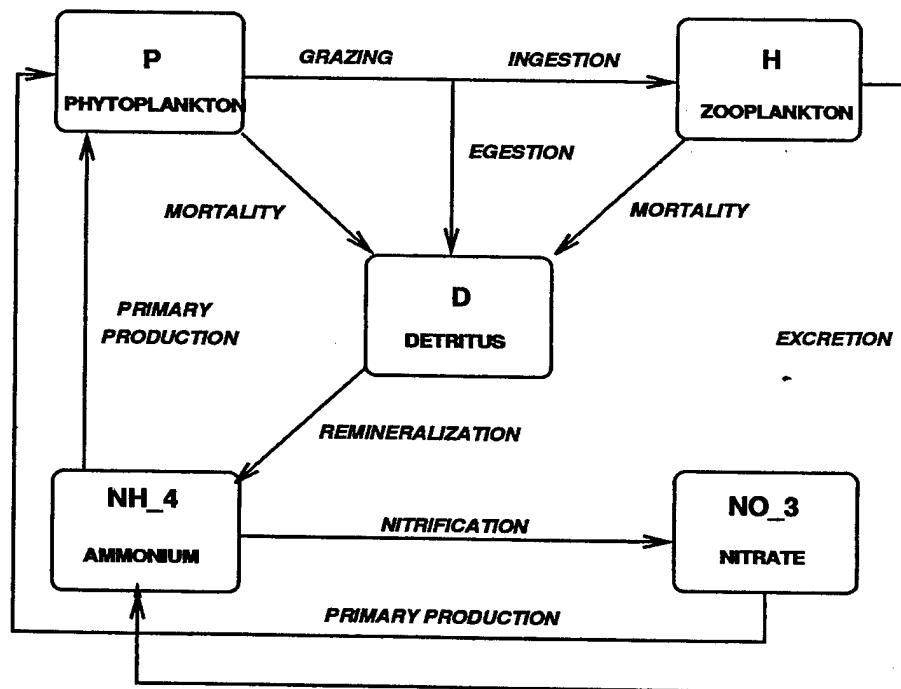
Figure 2-1: Schematic of the five-compartment biological model showing the flow pathways for nitrogen.

The local changes of the biochemical variables are described by

$$\frac{\partial B}{\partial t} = \frac{\partial}{\partial z}\left[(K_h + \nu_h)(\frac{\partial B}{\partial z})\right] + F_B \tag{2.1.9}$$

where B represents any of the five biological variables with P for phytoplankton biomass, H for herbivorous zooplankton biomass, D for pelagic detritus, N for nitrate and A for ammonium concentrations. F_B signifies the biological interaction terms for the equations of the five biological variables (e.g., Wroblewski, 1977; Fasham et al., 1990)

$$F_P = \Phi(I, N, A)P - G(P)H - m_p P \tag{2.1.10}$$

$$F_H = \gamma G(P)H - m_h H - \mu_h H \tag{2.1.11}$$

$$F_D = (1 - \gamma)G(P)H + m_p P + m_h H - \varepsilon D + w_s(\frac{\partial D}{\partial z}) \tag{2.1.12}$$

$$F_A = -\Phi_a(I, A)P + \mu_h H + \varepsilon D - \Omega A \tag{2.1.13}$$

$$F_N = -\Phi_n(I, N)P + \Omega A \tag{2.1.14}$$

where the definitions of the parameters and their default values are given in Table 2.1.

The total production of phytoplankton, $\Phi(I, N, A)$, is defined by

$$\Phi(I, N, A) = \sigma_m min[\alpha(I), \beta_t(N, A)] \tag{2.1.15}$$

17

	Definition	Value	Unites
f	Coriolis parameter	10^{-4}	s^{-1}
g	gravitational acceleration	9.81	ms^{-2}
ρ_0	reference density	1000	kgm^{-3}
c_p	specific heat of water	$4e^3$	$Jkg^{-1}c^{-1}$
κ	Von Karman constant	0.4	—
σ_m	maximum phytoplankton growth rate	0.75	day^{-1}
k_w	light extinction coefficient for PAR	0.03	m^{-1}
k_c	phytoplankton self-shading coefficient	0.03	$m^2(mmolN)^{-1}$
R_n	nitrate half-saturation constant	1	$mmolNm^{-3}$
R_a	ammonium half-saturation constant	0.8	$mmolNm^{-3}$
R_g	herbivore half-saturation constant	0.3	$mmolNm^{-3}$
a	photosynthesis efficiency parameter	0.05	$(wm^{-2})^{-1}$
m_p	phytoplankton death rate	0.05	day^{-1}
r_g	herbivore maximum grazing rate	0.21	day^{-1}
m_h	herbivore death rate	0.01	day^{-1}
μ_h	herbivore excretion rate	0.05	day^{-1}
ε	detrital remineralization rate	0.05	day^{-1}
Ω	ammonium oxidation rate	0.03	day^{-1}
w_s	detrital sinking rate	0.5	$mday^{-1}$
γ_h	herbivore assimilation efficiency	0.8	—
P_0	initial phytoplankton concentration	0.05	$mmolNm^{-3}$
H_0	initial herbivore concentration	0.1	$mmolNm^{-3}$
D_0	initial detritus concentration	0.05	$mmolNm^{-3}$
A_0	initial ammonium concentration	0.1	$mmolNm^{-3}$

Table 2.1: Parameter definitions and values for the default case. References: Wroblewiski et. al., 1988; Scott C. Doney et al, 1996; G. C. Hurtt et al, 1996; Oguz et al, 1996.

where *min* refers to the minimum of either $\alpha(I)$ or $\beta_t(N, A)$ representing the light limitation function and the total nitrogen limitation function of the phytoplankton uptake, respectively. Here $\beta_t(N, A)$ is given in the form

$$\beta_t(N, A) = \beta_n(N) + \beta_a(A) \tag{2.1.16}$$

with $\beta_a(A)$ and $\beta_n(N)$ signifying the contributions of the ammonium and nitrate limitations, respectively. They are expressed by the Michaelis-Menten uptake formulation

$$\beta_a(A) = \frac{A}{(R_a + A)} \tag{2.1.17}$$

$$\beta_n(N) = \frac{N}{(R_n + N)} exp(-\psi A) \tag{2.1.18}$$

where R_n and R_a are the half-saturation constants for nitrate and ammonium, respectively. The exponential term in the last of the above equations represents the inhibiting effect of ammonium concentration on nitrate uptake, with ψ signifying the inhibition parameter (Wroblewski, 1977).

The individual contributions of the nitrate and ammonium uptakes to the phytoplankton production are represented by, respectively, (c.f. Varela et al., 1992)

$$\Phi_n(I, N) = \sigma_m min[\alpha(I), \beta_t(N, A)](\beta_n/\beta_t) \tag{2.1.19}$$

$$\Phi_a(I, A) = \sigma_m min[\alpha(I), \beta_t(N, A)](\beta_a/\beta_t) \tag{2.1.20}$$

The light limitation is parameterized according to Jassby and Platt (1976) by

$$\alpha(I) = tanh[aI(z, t)] \tag{2.1.21}$$

$$I(z, t) = I_s exp[-(k_w + k_c P)z] \tag{2.1.22}$$

19

where a denotes photosynthesis efficiency parameter controlling the slope of $\alpha(I)$ versus the irradiance curve at low values of the photosynthetically active irradiance (PAR). I_s denotes the surface intensity of the PAR which is taken as 0.45 of the climatological incoming solar radiation from the data.

The zooplankton grazing ability is represented by the Michaelis-Menten formulation

$$G(P) = \sigma_g \frac{P}{(R_g + P)} \tag{2.1.23}$$

For phytoplankton, zooplankton, nitrate and ammonium the boundary conditions at the surface and bottom are given by an equation of the form

$$(K_h + \nu_h)\frac{\partial B}{\partial z} = 0 \quad \text{at} \quad z = 0, \; z = -D \tag{2.1.24}$$

For the detritus equation the surface boundary condition is modified to include the downward sinking flux

$$(K_h + \nu_h)\frac{\partial D}{\partial z} + w_s D = 0 \quad \text{at} \quad z = 0 \tag{2.1.25}$$

The same condition is also prescribed at the lower boundary of the model which is taken at 400 m depth, well below the euphotic zone. Our choice of the sinking rate is relatively low ($w_s = 0.5 \; m/day$, Table 2.1). The advantage of locating the bottom boundary at considerable distance away from the euphotic layer is to allow the complete remineralization of the detrital material until it reaches the lower bounday of the model and the vertically integrated biological model is fully conservative.

20

2.2 The seasonal variability of the upper layer physics and biology of the Sargasso Sea: response to physical forcings in the default case

The annual variations of the wind stress and heat flux components are expressed by smooth, climatological surface forcing functions (Doney et al., 1996)

$$F = Mean + Amplitude \cdot \cos(2\pi \frac{t}{365} - phase) \qquad (2.2.26)$$

where time, t, is given in days. The annual means, seasonal amplitudes, and phases as shown in Table 2.2 are computed from climatological data sets (Esbensen and Kushnir, 1981; Isemer and Hasse, 1985) for the region of the BATS site (31°50'N and 64°10'W).

	Units	Annual Mean	Amplitude	Phase (^{o})
Wind stress	(N/m^2)	0.081	0.040	60
Net longwave	(W/m^2)	-60.0	5.0	70
Sensible heat	(W/m^2)	-26.0	22.0	170
Latent heat	(W/m^2)	-162.5	90.0	170
Solar	(W/m^2)	198.7	–	–

Table 2.2: Climatological physical forcing functions for reference case

The surface wind stress (Fig. 2-2 (c)) peaks at 1.2 $dyn cm^{-2}$ in March, and the annual mean heat loss from the non-solar terms is 248.5 wm^{-2} with a maximum of 365.5 wm^{-2} in late December. Solar radiation is computed with a constant cloud fraction of 0.75, which leads to an annual mean solar heating rate of 198.7 wm^{-2} that is within the reported climatological range of $180 - 200$ wm^{-2} (Esbensen and Knshnir, 1981). The required cloud fraction, however, is slightly higher than the

climatological value of approximatly 0.6 near Bermuda (Warren et al., 1988). The annual heat budget at Bermuda is not closed locally by air-sea exchange (the dashed line in Fig. 2-2 (a)), therefore, an excess heat flux at the surface is added in our model in order to run stable, multi-year integrations. The surface heat flux function we used to force the model is the solid line in Figure 2-2 (a).
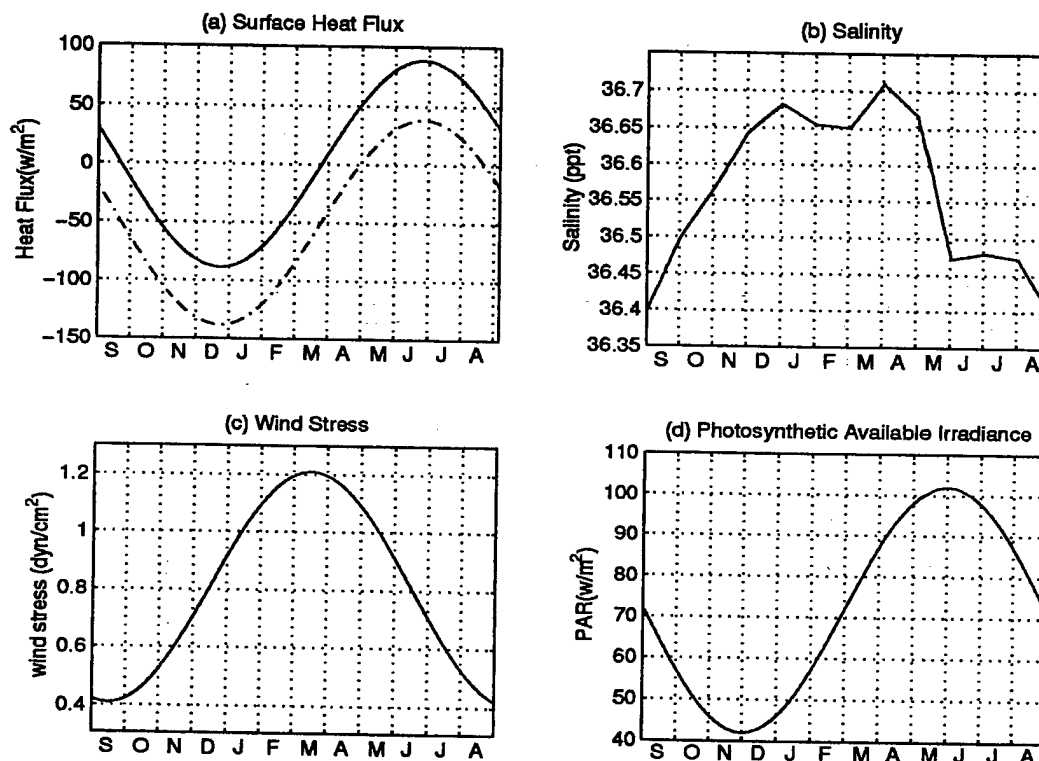
Figure 2-2: The annual variations of the surface boundary conditions used in the model.

The surface salinity values were derived by the linear interpolation of the mean monthly CTD data over the upper 8 meter of the ocean (Levitus, 1994). As shown in Figure 2-2 (b), it has greatest values during the winter and early spring with a maximum value of 36.7, and lowest values during the summer with a minimum value of 36.4. The photosynthetic Available Irradiance (PAR) variations (Fig. 2-2 (d)) were the climatological data from Word Ocean Atlas (1994). The PAR is expressed as a

harmonic function with amplitude 30 wm^{-2} and centered at 70 wm^{-2} on February 28.

The model temperature and salinity profiles are initialized with the Levitus 94 data in September as shown in Figure 2-3 (a) and (b), respectively. The biological simulations are initialized with a uniform nitrate concentration of 0.3 $mmolNm^{-3}$ over the mixed layer (0-150 m), increasing linearly below that depth to 6.0 $mmolNm^{-3}$ at 400 m (Fig. 2-3 (c)).
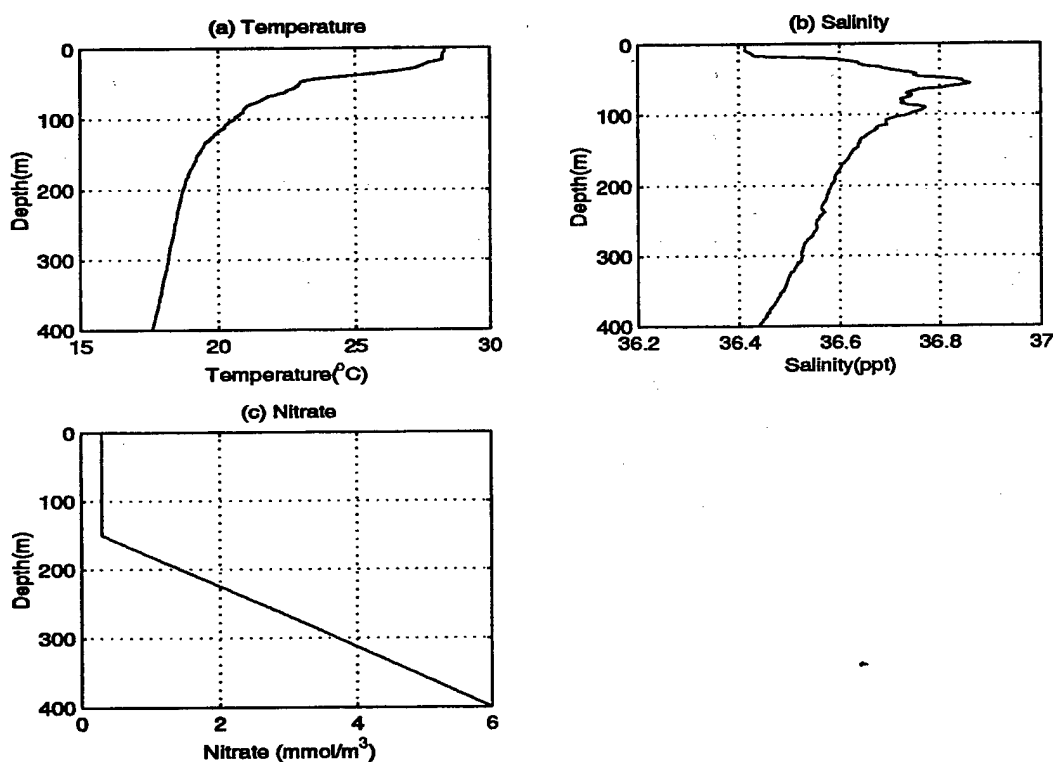
Figure 2-3: The initial conditions used in the model.

The model equations are solved using the finite difference procedure decribed by Mellor (1990). A total of 27 vertical levels are used for the water column of 400 m depth. The grid spacing is compressed slightly toward the surface to increase the resolution within the uppermost levels. The numerical scheme is implicit to avoid

computational instabilities associated with the small vertical grid spacing. Aselin filter (1972) is applied at every time step to avoid time splitting due to the leapfrog time scheme. A time step of 10 minutes is used in the numerical integration of the equations.

First, the physical model is integrated for 5 years. An steady state with repeating yearly cycle of the dynamics is obtained after 3 years of integration in this system. Then using the fifth year solution of the physical model, the biological model is integrated for 4 years to obtain the repetitive yearly cycles of the biological variables. The depth integrated total nitrogen content, $N_t = N + A + P + Z + D$, should remain a constant value over the annual cycle when the equilibrium state is obtained.

2.2.1 The upper layer physical structure

The yearly response of the upper layer physical structure to the forcing functions is shown in Figure 2-4. The winter is characterized with strong cooling and deep mixed layer, especially in February and March, the mixed layer depth exceeds 220 m and the mixed layer temperature is about 19.5^oC. Accordingly, there are high values of eddy diffusivity during the same period (Fig. 2-4 (c)). After mid-April, as the water column warms up gradually, the mixed layer depth decreases. During the summer, due to the weak mixing associated with the weak wind stress forcing and the strong heating, the surface temperature increases upto a maximum value of 27^oC, the mixed layer shoals to less than 10 m deep, and a sharp seasonal thermocline system at the base of the mixed layer is developed. The wind-induced, weak and shallow mixed layer characteristics are consistent with the low values of eddy diffusity shown in Figure 2-4 (c). The autumn period is characteristic with mixed layer depth of 50-75 m and temperature of around 22^oC, salanity around 36.575. This is then followed by the deeper penetration of the mixed layer and subsequent cold water mass formation
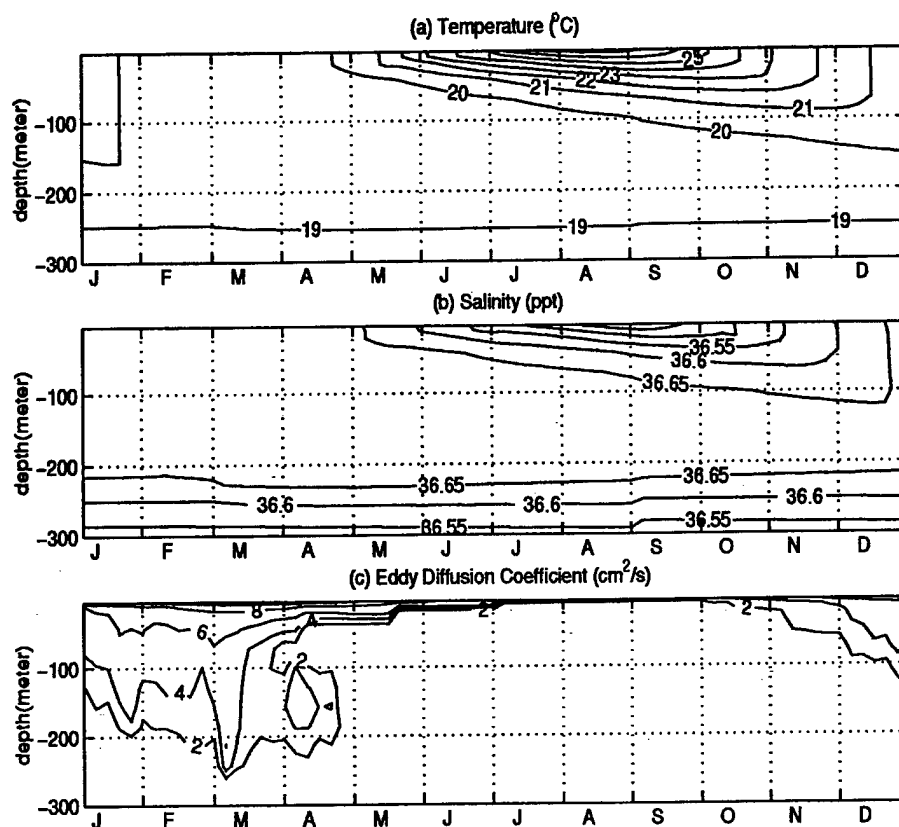
Figure 2-4: The depth and time variations of the (a) temperature (^oC), (b)salinity (ppt) and (c) eddy diffusion coefficient (cm^2/s).

as a result of the strong cooling in January and February.

2.2.2 The upper layer biological structure

The temporal and vertical distributions of the five biochemical variables are shown in Figure 2-5. In agreement with the physical structure of the upper ocean, there are several phases of the biological structure within the year. Due to the deep convection in the winter, the surface layer is enriched with nutrients entrained from below. The mixed layer nitrogen concentration then increases gradually to its maximum values in April. The phytoplankton bloom starts to develop as a result of nutrient enrich-

ment and sufficient light availability during January and reaches the maximum level in March and April. In this period, as a result of strong vertical mixing generated by the winter convective overturning mechanism, the water column is overturned completely and the deepest and coolest mixed layer formation is established. The spring phytoplankton growth process takes place during March and April and remains until June. The summer and fall periods are characterised by the nutrient depletion and low phytoplankton production in the mixed layer. The phytoplankton biomass is low because, with weak convection, the nutrient supply from the nutrient rich water below the mixed layer is no longer possible and the phytoplankton biomass is consumed by the herbivore in the surface waters. In the summer, the stratification and the subsequent formation of the strong seasonal thermocline inhibit nutrient flux into the shallow mixed layer from below, so nutrient limitation prohibits the development of bloom during the summer season. The nitrate concentrations below the seasonal thermocline increase and together with sufficient light availability, lead to the surface maximum of phytoplankton biomass in the layer between the seasonal thermocline and the base of the euphotic zone during July and August. Remineralization of the particulate organic material following degradation of the spring bloom produces ammonium. A part of the ammonium is used in the regenerated production and the rest is converted to the nitrate through the nitrification process. The yearly distributions of zooplankton and detritus follow closely that of phytoplankton with a time lag of approximately two weeks. The maximum zooplankton concentrations occur following the phytoplankton spring blooms as well as the period of summer subsurface phytoplankton maximum, respectively.
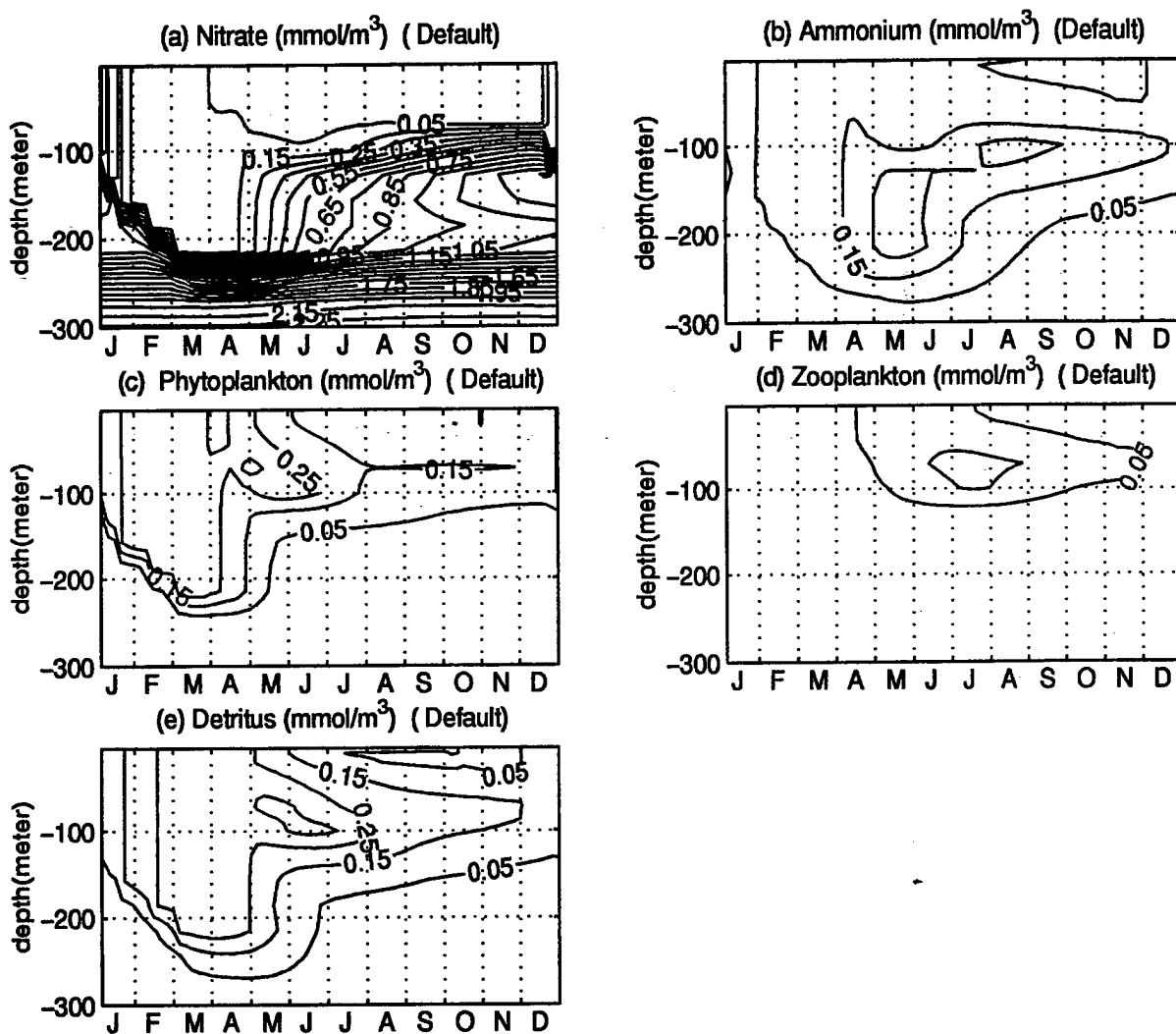
Figure 2-5: The depth and time variations of the (a)nitrate, (b)ammonium, (c)phytoplankton, (d)zooplankton and (e)detritus.

2.2.3 Dynamics of the phytoplankton blooms.

In this section, we describe briefly the main mechanisms controlling the initiation, development and degradation of the bloom, as well as the subsurface maximum of the summer season. First, we consider the relative roles of light and nutrient uptake in the primary production process. The control of the phytoplankton growth by either light or nutrient limitation during the year is shown in Figures 2-6 (a) and (b). In Figure 2-6 (b) relatively high gradient region at about 50-100 m deep separates the low nitrogen limitation region near the surface from the region of high values below during the summer. The light limitation function has the opposite structure with decreasing values towards the deeper levels (Fig. 2-6 (a)). Therefore, the net growth function (Fig. 2-6 (c)), which is the minimum of these two, is generally governed by the nitrogen limitation near the surface and by the light limitation at deeper levels. A subsurface maximum is present at the depths of about 50-100 m where they both have the moderate values. During the summer season, this is responsible for the subsurface phytoplankton production.

From Figure 2-6 (c) we note that the highest values of the net growth function within the upper 50 m layer occur during January and February. But the bloom develops at a later time, at the end of March (Fig. 2-5 (c)). There are two dynamical reasons for the absence of the bloom generation in the midwinter period. First, although the net growth function has high values, the amount of phytoplankton biomass at that time is not sufficient to initiate the bloom. Second, the surface layer has relatively strong downward diffusion (see Fig. 2-4 (c)), which counteracts against the primary production and therefore prevents the bloom development. However, as soon as the intensity of the vertical mixing diminishes in April, a new balance is established. The time change term (Fig. 2-7 (d)) reaches maximum at the surface at the beginning of April and subsurface maximum in the late half of April. This new

28
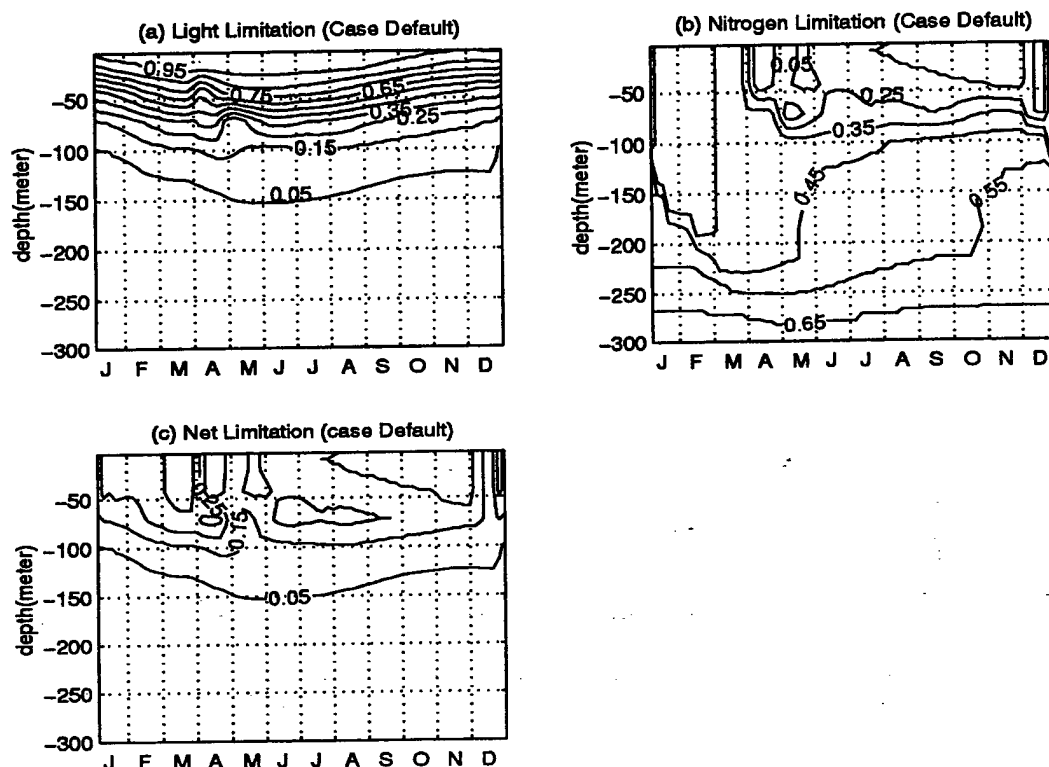
Figure 2-6: The depth and time variations of the (a)nondimensional nutrient limitation function, (b)nondimensional nutrient limitation function and (c)the net limitation function within the year.

balance leads to an exponential growth of the phytoplankton concentration in the mixed layer. Soon after the initiation phase, the zooplankton grazing (Fig. 2-7 (c)) starts dominating the system and balances the primary production. This continues until the nitrate stocks in the mixed layer are depleted and the nitrate-based primary production (new production) (Fig. 2-7 (a)) weakens. At the same time, rapid recycling of the particulate material allows for the ammonium-based regenerated production (Fig. 2-7 (b)), which also contributes to the bloom development. The bloom terminates abruptly towards the end of May when the ammonium stocks are also no longer enough for the regenerated production.

The downward diffusion process mentioned above is evident in the period from

29

January to April with values of K_h greater than $2\ cm^2/s$ in the mixed layer (see Fig. 2-4 (c)). The termination of the convective mixing process in late April is implied in Fig. 2-4 (c) by a sudden an order of maginitude reduction in the K_h values. Shown further in Figures 2-4 (a) and 2-5 (c) is that the period of high K_h values is identified with the vertically uniform temperature structure of about 19.5^oC and the phytoplankton structure of approximately $0.3\ mmolNm^{-3}$. Following the termination of convective overturning, the subsurface stratification begins establishing. As the mixed layer temperature increases by about 0.5^oC (from 19.5 to 20^oC), the phytoplankton bloom attains its peak amplitude ($3.5\ mmolNm^{-3}$) within the next half month.
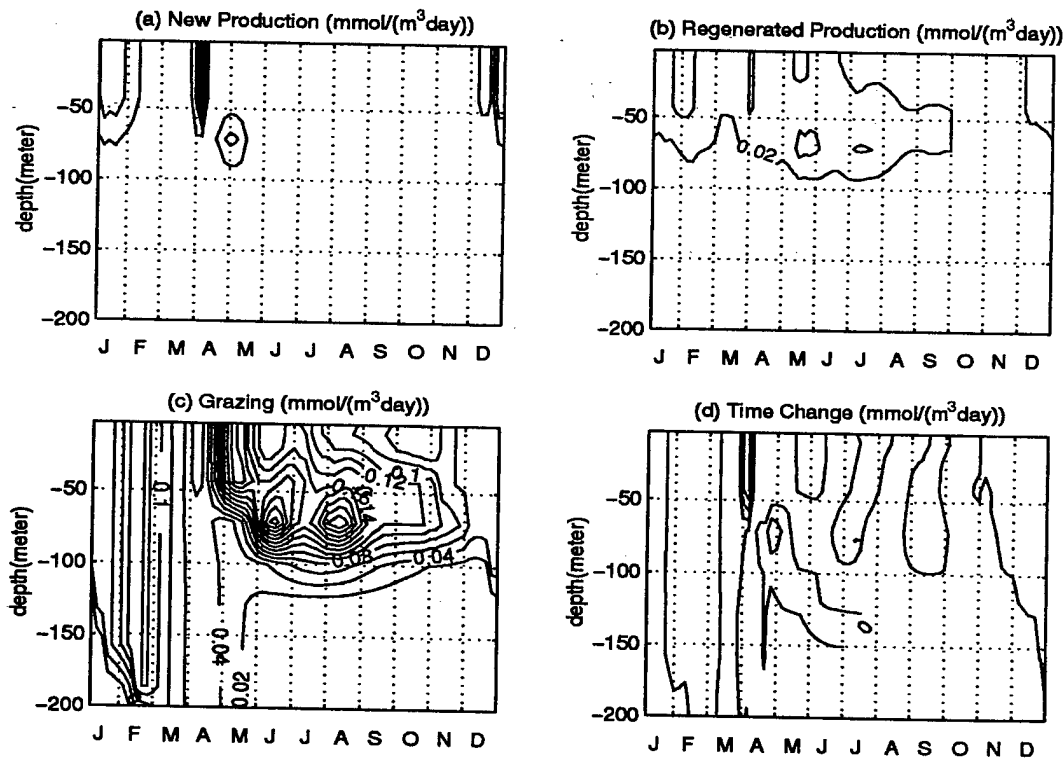
Figure 2-7: The depth and time variations of the (a) new production, (b) regenerated production, (c) zooplankton grazing and (d) time change of phytoplankton.

2.3 Sensitivity experiments of biochemical parameters.

A series of experiments are carried out to analyse the sensitivity of the model to the externally specified parameters (see Table 2.1). The experiments and the parameter values, which are changed for each experiment, are listed in Table 2.3. The experiments show that if the variation of one parameter affects the distribution of phytoplankton, it affects phytoplankton even more drastically. The important parameters that affect the structure of phytoplankton, and therefore zooplankton, are phytoplankton maximum growth rate σ_m, phytoplankton death rate m_p, light extinction coefficient for PAR k_w, nitrate half-saturation constant R_n, herbivore maximum grazing rate r_g, herbivore death rate m_h, herbivore excretion rate μ_h, herbivore assimilation efficiency γ_h, herbivore half-saturation constant R_g, detrital remineralization rate ε, and detrital sinking rate w_s. The bloom structure does not change much when the values of phytoplankton self-shading coefficient k_c, ammonium half-saturation constant R_a, photosynthesis efficiency parameter a, and ammonium oxidation rate Ω vary. A few examples are presented to give an idea of how the settings of the biological parameters affect phytoplankton and zooplankton.

Tests of the extinction coefficient of PAR (default value $k_w = 0.03\ m^{-1}$).
As shown in Table 2.3, two experiments were carried out according to this parameter. We ran the model with the value of $k_w = 0.06\ m^{-1}$ in experiment C1 and $k_w = 0.015\ m^{-1}$ in experiment C2. An increase to the default value of k_w intensifies the distribution of phytoplankton and zooplankton towards the sea surface (Fig. 2-8 (c) and (d)). Lowering its value, the distributions of phytoplankton and zooplankton are stretched into the deeper water (Fig. 2-9 (c) and (d)). In our model, phytoplank-

31

	σ_m	m_p	k_w	k_c	R_a	R_n	R_g	a	r_g	m_h	μ_h	γ_h	ϵ	Ω	w_s
df	.75	.05	.03	.03	.8	1	.3	.05	.21	.01	.05	.8	.05	.03	.5
A1	1.5														
A2	.375														
B1		.1													
B2		.025													
C1			.06												
C2			.015												
D1				.06											
D2				.015											
E1					1.6										
E2					.4										
F1						2									
F2						.5									
G1							.6								
G2							.15								
H1								.1							
H2								.25							
I1									.42						
I2									.105						
J1										.02					
J2										.005					
K1											.1				
K2											.025				
L1												1.6			
L2												.4			
M1													.1		
M2													.025		
N1														.06	
N2														.015	
O1															3
O2															.025

Table 2.3: Parameter values for the sensitivity experiments. The line "df" stands for the deafult values. If the value is not defined it is the same as the default.
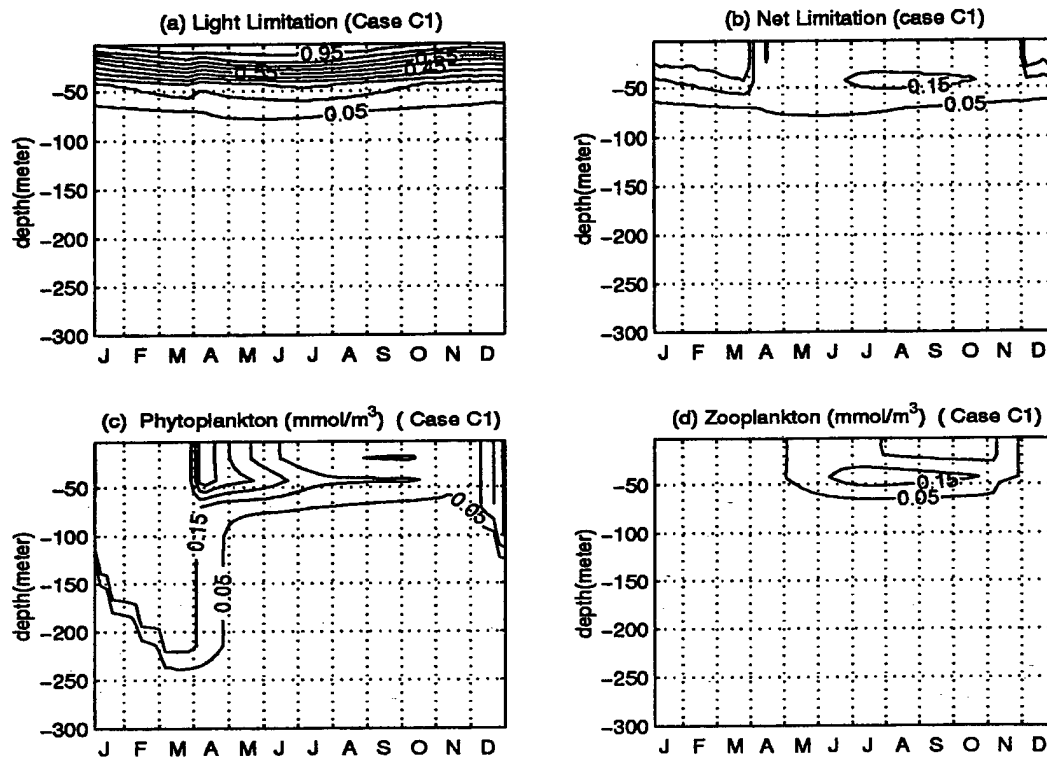
Figure 2-8: The depth and time variations in Case C1 of the (a)light limitation function, (b)the net limitation function, (c)phytoplankton and (d)zooplankton within the year.

ton growth rate depends on the minimum of nutrient limitation and light limitation. As decribed in section 1.3.3, it is governed by the nitrogen limitation near the surface and by the light limitation at deeper levels. Comparing the light limitation in Figure 2-8 (a) with Figure 2-6 (a), we see that the light limitation in case C1 decreases except in the very near surface region. The most striking difference is that in the deafult case, the 0.05 contour of light limitation ranges from 100 to 150 meter in depth, while in case C1, it is between 66 and 84 meter. The subsurface maximum of net limitation decreases and shifts towards the sea surface except in the winter. Therefore, the distribution of phyoplankton is squeezed towards the sea surface when it is not in the winter. Zooplankton, which feeds on phytoplankton, also moves its
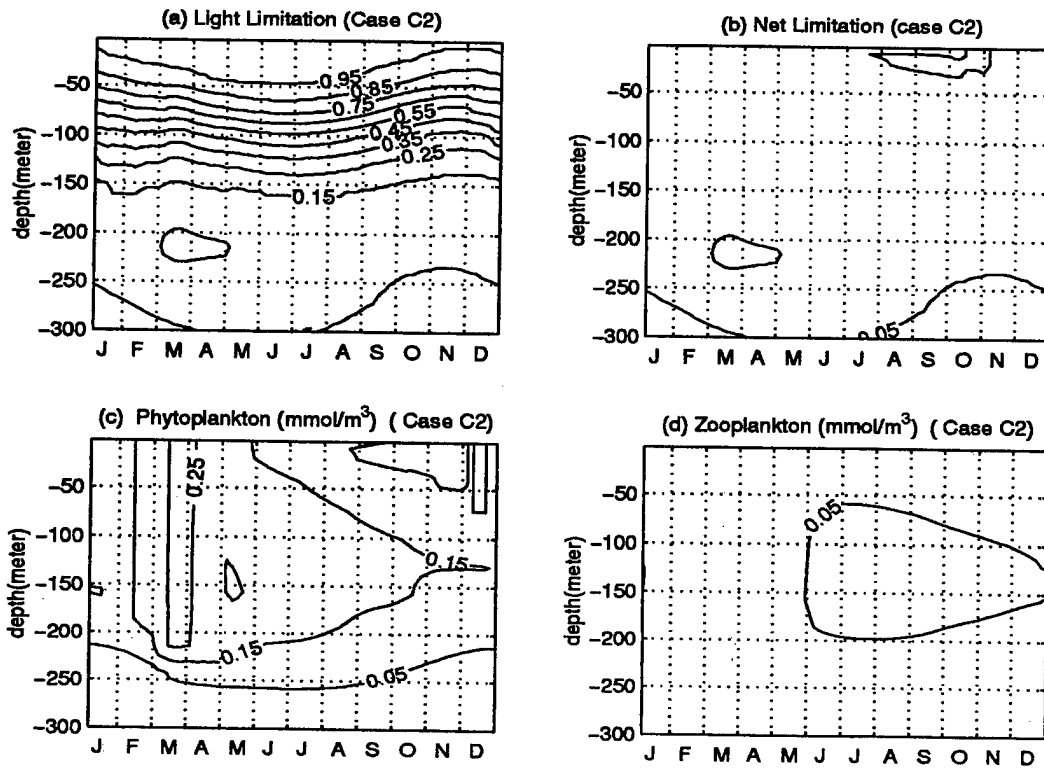
Figure 2-9: The depth and time variations in Case C2 of the (a)light limitation function, (b)the net limitation function, (c)phytoplankton and (d)zooplankton within the year.

distribution about 50 meter closer to the seasurface than in the default case. The dynamics in case C2 is opposite to that in case C1.

Tests of the nitrate half saturation coefficient (default $R_n = 1 \; mmmolNm^{-3}$).

If algae are placed in a nutrient medium, the concentration of nutrients decreases over time in the medium as they are incorporated into the plant cells. The velocity at which algae uptake removes nutrients depends on the nutrient concentration in the medium (Valiela, 1995). Uptake rates of nitrate or ammonium by phytoplankton give hyperbolas when graphed against the nitrate or ammonium concentration in the environment (Eppley, 1969). In the Michaelis-Menten equation, the half saturation

constant reflects the relative ability of phytoplankton to use low levels of nutrients and thus may be of ecological significance. In the case of nitrate, nutrient uptake occurs in two steps: first, nutrients are taken into the phytoplankton cell at a rate determined by the ambient nutrient concentration; then, as the concentration inside of the cell increases, the nutrient is utilized in proportion to the internal cellular concentration and not the external ambient concentration. If the nitrate uptake rate is measured when ammonium is present, the uptake of nitrate maybe severely underestimated because of the preference for ammonium by many algae. The half saturation constant is high in more euphotic and nutrient-rich water and low in oligotrophic waters.

Two experiments were carried out: $R_n = 2 \, mmmolNm^{-3}$ in case F1 and $R_n = 0.5 \, mmmolNm^{-3}$ in case F2. Increasing the value of R_n in case F1 increases the values and elongates the durance of the phytoplankton spring bloom (Fig. 2-10 (a) and (b)). The subsurface maximum of phytoplankton now extends into July, while in the default case it extends into June. However, zooplankton has only weak distribution which spans from July to November in the upper 120 meter. Opposite results were obtained when the value of R_n was decreased in case F2 (Fig. 2-10 (c) and (d)).

Tests of the detrital sinking rate (default $w_s = 0.5 \, mday^{-1}$).

The sinking rate of the particulate organic matter, w_s, is one of the most critical parameters in the model. The value of w_s appropriate for the model simulations is 0.5 $mday^{-1}$, which implies that the faster sinking, larger particles do not contribute to the processes taking place within the euphotic zone. The choice of greater values causes faster sinking of the detrital material toward the deeper levels, thereby decreasing the detritus and subsquently the nitrogen concentrations in the euphotic layer. The sinking material thus effectively becomes lost from the euphotic zone. Figure 2-11 (a) and (b) show the results of the model run when the sinking velocity is taken as 3 $mday^{-1}$, and (c) and (d) show the results when the sinking velocity is 0.025
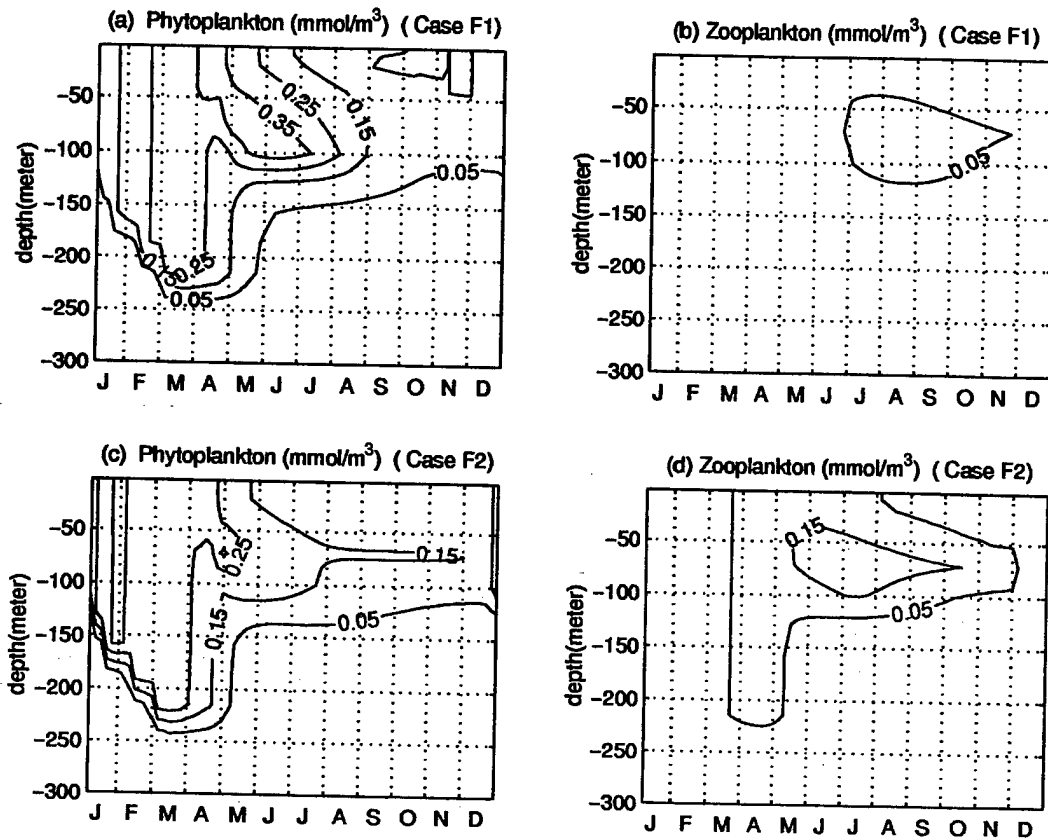
Figure 2-10: The depth and time variations of the (a)phytoplankton and (b)zooplankton of Case F1; (a)phytoplankton and (b)zooplankton of Case F2.

$mday^{-1}$. The change in the value of w_s alters the whole biological system drastically. In case O1 ($w_s = 3\ mday^{-1}$), there exists only a weak bloom in April and May (Fig. 2-11 (a)), with almost no zooplankton biomass and detritus in the study area. The euphotic layer is depleted in both ammonium and nitrate, which are, accumulated at deeper levels. The case with $w_s = 0.025\ mday^{-1}$ allows a more than complete remineralization of the detrital material before it reaches the lower bounday of the model. Upon the decrease of the value of w_s, the concentrations of phytoplankton and zooplankton are higher than in the default case as shown in Figure 2-11 (c) and (d), especially during the winter when the complete overturning of the water column

provides richer supply of nutrients in the euphotic zone.
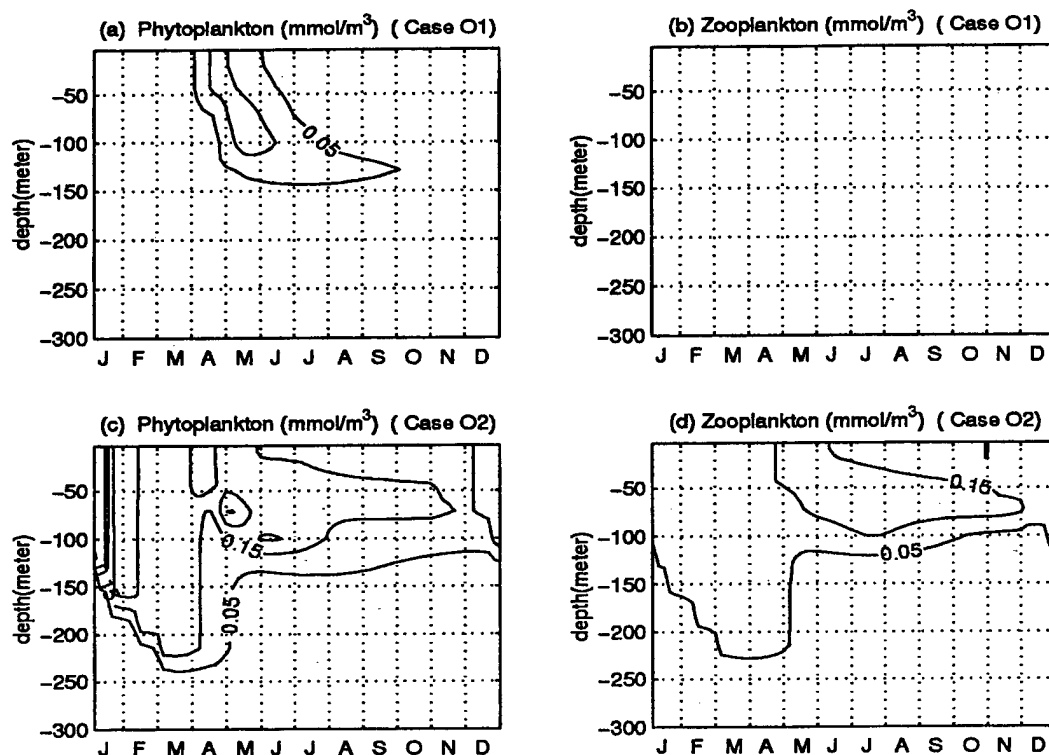
Figure 2-11: The depth and time variations of the (a)phytoplankton and (b)zooplankton of Case O1; (c)phytoplankton and (d)zooplankton of Case O2.

2.4 Comparison of model results with BATS observations.

The model solutions of temperature and salinity (Fig. 2-4) correspond well with the climatological data (1961-1970) in Figure 2-12 from Hydrostation S (WHOI and BBSR, 1988; Musgrave et al., 1988). They also compare quite well with the model results of Doney et al., 1996. The model simulations exhibit the characteristic deep winter convective depth, shallow summer mixed layer and sharp seasonal thermocline

found in the data. The seasonal salinity cycle also generally agrees with climatology, showing the greatest salinities during the winter convection period and the formation of a fresh surface layer over the summer. A sub-surface salinity maximum ($S > 36.6$) appears in both the model solution and the observation.
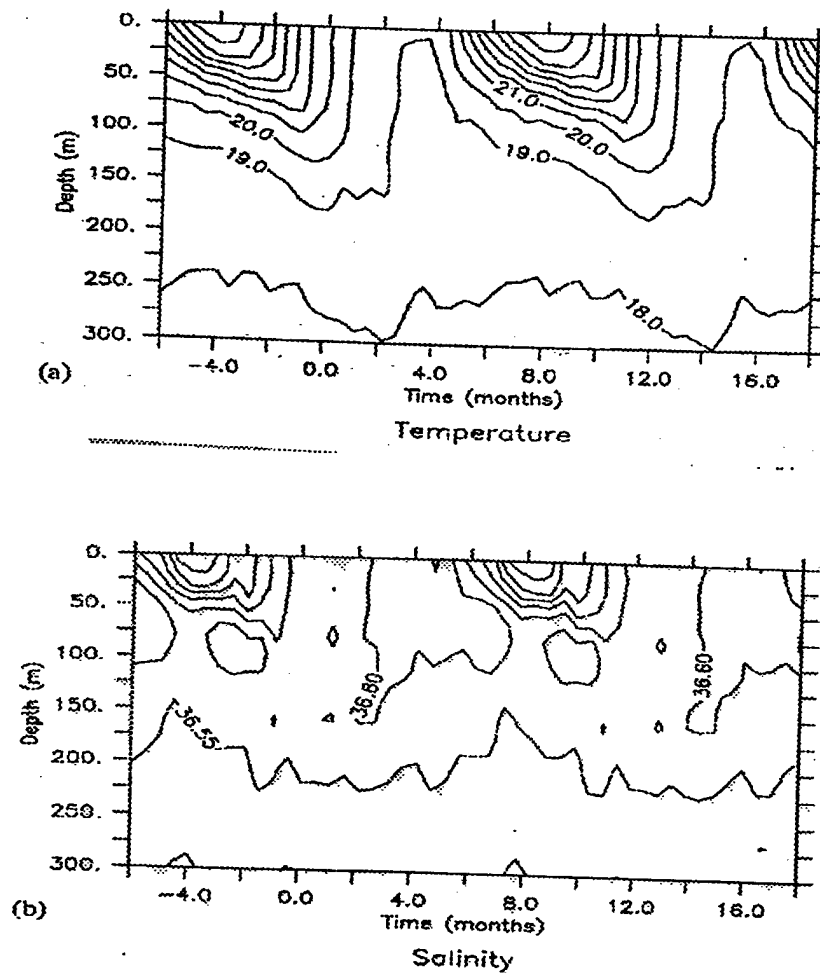
Figure 2-12: Climatological (1961-1970) seasonable cycles of (a) temperature (^oC) and (b) salinity for Hydrostation S.

Our model is driven with a uniform nitrate concentration of 0.3 $mmolNm^{-3}$ over the mixed layer ($0 - 150\ m$), increasing linearly below that depth to 6.0 $mmolNm^{-3}$ at 400 m. A direct comparision of the coupled model and the data is difficult because

the BATS data contains considerable interannual variability and is currently of insufficient length to generate a true biological climatology. The smooth climatological forcing has the likely effect on the model solutions of reducing variability of deep convection during the winter, causing greater homogenization of properties over the winter mixed layer depth, and weakening individual bloom events driven by short-term variability. The monthly climatologies in Figure 2-13 of nitrate was created from the first four years of BATS (1988-1992) (Knap et al., 1991, 1992, 1993). The climatologies are useful for judging the general character of the model solutions, but quantitative comparison should be limited to more robust features of the biological seasonal cycle. The model nitrate field agrees reasonablly well with the BATS field data. The surface winter concentrations are about 0.2 $mmolNm^{-3}$ and the depth of the summer nitracline is about 100-125 m. The approximately uniform concentrations in the deep winter mixed-layer gradually increase over the summer due to the remineralization of detritus. However, in the model result the nitrate values are generally lower than that observed.
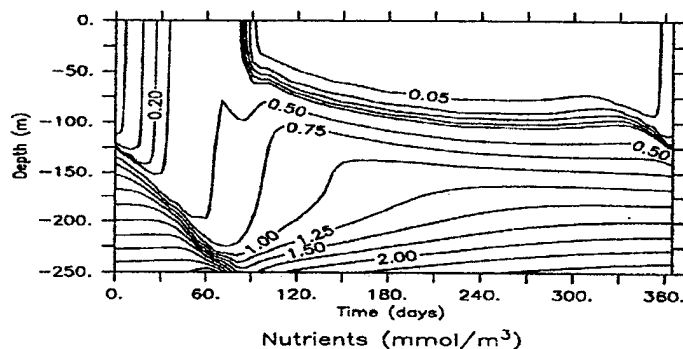
Figure 2-13: Climatological seasonale cycle of nitrate for the first 4 years 1988-1992 of the BATS record (Knap et al., 1991, 1992, 1993)

Chapter 3

Observation of phytoplankton Chlorophyll a in the Gulf of Maine - Georges Bank region

3.1 Methods

3.1.1 Study area and data source

Our study area includes the Gulf of Maine, Georges Bank and a small part of the Middle Atlantic Bight that is north of 39°N (Fig. 3-1, O'Reilly and Zetlin, 1996). In this thesis, the expression "North Middle Atlantic Bight" will be used to refer to the small area north of 39°N on the Middle Atlantic Bight. The Gulf of Maine, Georges Bank and the Middle Atlantic Bight constitute the three major subdivisions of the Northeast U.S. continental shelf, with different bottom topographies (Fig. 3-2, O'Reilly and Zetlin, 1996). The Gulf of Maine, a semi-enclosed continental shelf sea, is bounded by the northeast U.S. and Nova Scotia coasts and includes waters west of longitude 66°W between Georges Bank and the entrance of the Bay of Fundy.

The bottom depth throughout much of the Gulf of Maine is greater than 100 m and averages 150 m (Uchupi and Austin, 1987). There are three large basins, the Georges Basin, Wilkinson Basin and Jordan Basin and several smaller ones. Shallow water (of depth less than 60 m) is mostly confined to a relatively narrow band along the coast and on Stellwagen Bank which is west of the Jordan Basin and north of Cape Cod. Georges Bank is generally limited by the 200 m isobath except in the west and northwest. From Georges Basin to Georges Bank the water shoals quickly from 200 m to 60 m within a relatively short distance, less than 30 km. The eastern and southern extent are defined by the Northeast Channel and the shelf-break. The Middle Atlantic Bight includes the shelf area between Cape Hatteras and the Great South Channel. The shelf here slopes gently offshore and is shallow compared with the Gulf of Maine and Georges Bank.

The concentration of Chlorophyll a, the dominant photosynthetic pigment in phytoplankton, is widely used by biological oceanographers as a proxy for phytoplankton biomass. The data of concentration of Chlorophyll a were collected from the Marine Resources Monitoring, Assessment and Prediction program (MAPMAP) of the National Oceanographic and Atmospheric Administration, Northeast Fisheries Science Center between 1977 and 1988. Most of the Chlorophyll a data were obtained from more than five thousand hydrocasts profiles of the upper 100 m of the water column. The MARMAP surveys occupied up to 193 standard sites. In our study area we used stations 64 to 193. The station locations are shown in Figure 3-3 (O'Reilly and Zetlin, 1996). The coordinates of the 193 MARMAP stations were used to define the standard locations. Tiles (Green and Sibson, 1978) or Dirichlet cells (Ripley, 1981) were constructed around each standard location as shown in Figure 3-4 (O'Reilly and Zetlin, 1996). The average distance between the standard MARMAP coordinates defining the 193 tiles is of 42 km.

The data are the mean Chlorophyll a concentrations over a 2-month period (from
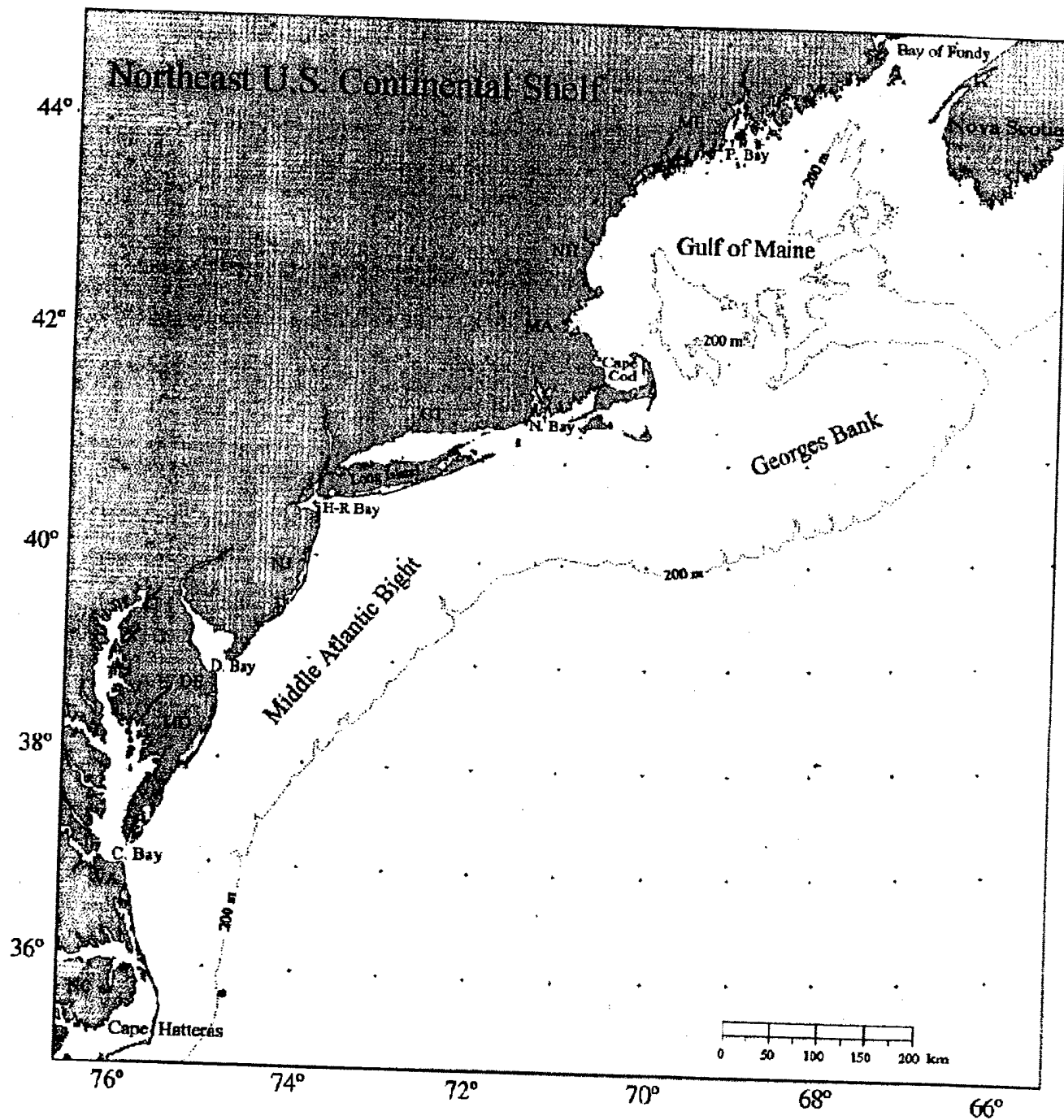
Figure 3-1: Northeast U.S. continental shelf (reproduced from O'Reilly and Zetlin, 1996)
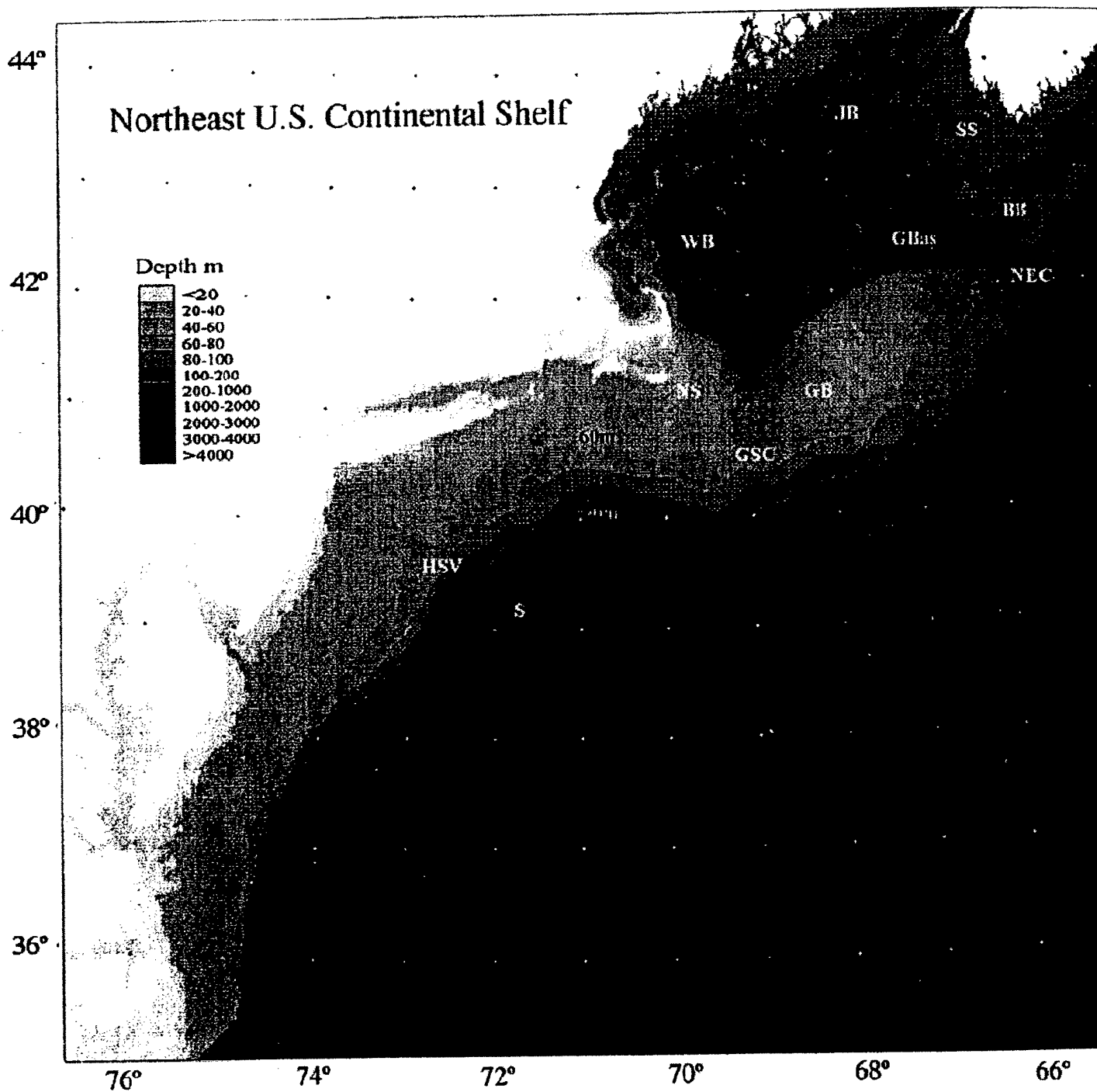
Figure 3-2: Bottom topography of the shelf (reproduced from O'Reilly and Zetlin, 1996)

43
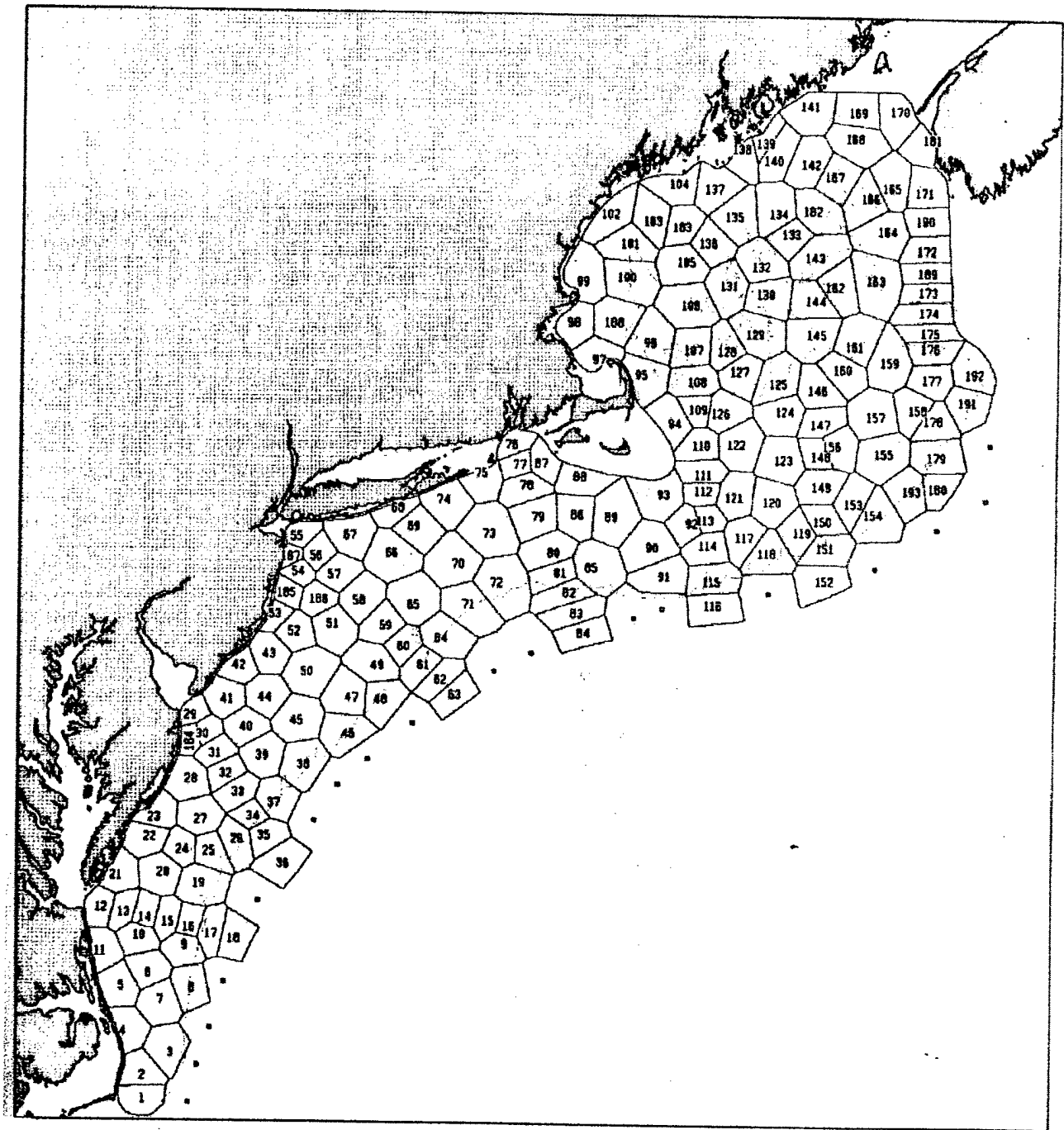
Figure 3-3: Stations and subdivisions of the shelf (reproduced from O'Reilly and Zetlin, 1996)

Gulf of Maine ~Depth (m)

●	Western	60-100
◉	Northern	80-200
◯	Wilkinson Basin	100-250
◯	Georges Basin	150-250
○	Jordan Basin	150-250
•	Scotian Shelf	60-200

Georges Bank ~Depth (m)

▴	Northern Shoals	30-40
▲	Central Shoals	35-55
N	Nantucket Shoals	37
◭	Western Outer Shoals	50-60
◮	Eastern Outer Shoals	60-80
△	Great South Channel	60-100
✳	Northeast Peak	80-200
△	Southern Flank	60-200
∥	Northern Slope	200-2000

Middle Atlantic Bight ~Depth (m)

c	Chesapeake Plume	14
D	Delaware Plume	20
H	Hudson-Rariton Plume	23
✕	Southern Nearshore	15-20
■	Central Nearshore	15-30
+	Southern Midshelf	20-40
▫	Central Midshelf	30-60
◇	Northern Midshelf	30-60
□	Southern Outer Shelf	60-200
◇	Northern Outer Shelf	60-200
∥	Southern Slope	200-2000

Figure 3-4: Map of Tiles (reproduced from O'Reilly and Zetlin, 1996)

45

Jan-Feb to Nov-Dec), by tile, and by depth for the Gulf of Maine-Georges Bank region.

3.1.2 OAX - optimal linear estimation

Since the data set is not uniform neither in spatial nor in temporal coverage, it is necessary to interpolate the irregular data both in space and in time. The OAX software package (see http://aimsirl.bio.dfo.ca/channah/oax.demo.html, by Charles Hannah, Mary Jo Graca and John Loder, 1995) is used for the optimal linear estimation. Distant (space or time) observations have little influence on an estimate when compared to nearby points and we choose only the best subset of data points that have the highest correlation, i.e. lowest error with the interpolation point. So OAX optimal linear estimation is a correlation weighted linear combination of a finite number ($num\_closest$) of nearest data points.

We suppose that at a data point X_n the measured value ϕ_n is the true value $\theta(X_n)$ plus some random noise ϵ_n:

$$\phi_n = \theta(X_n) + \epsilon_n \quad n = 1, 2, ..., num\_closest \qquad (3.1.1)$$

And the linear estimate at grid point X is a sum of the weighted measured values at $num\_closest$ data points:

$$\tilde{\theta}_X = \sum_{n=1}^{num\_closest} \alpha_{X_n} \phi_n \qquad (3.1.2)$$
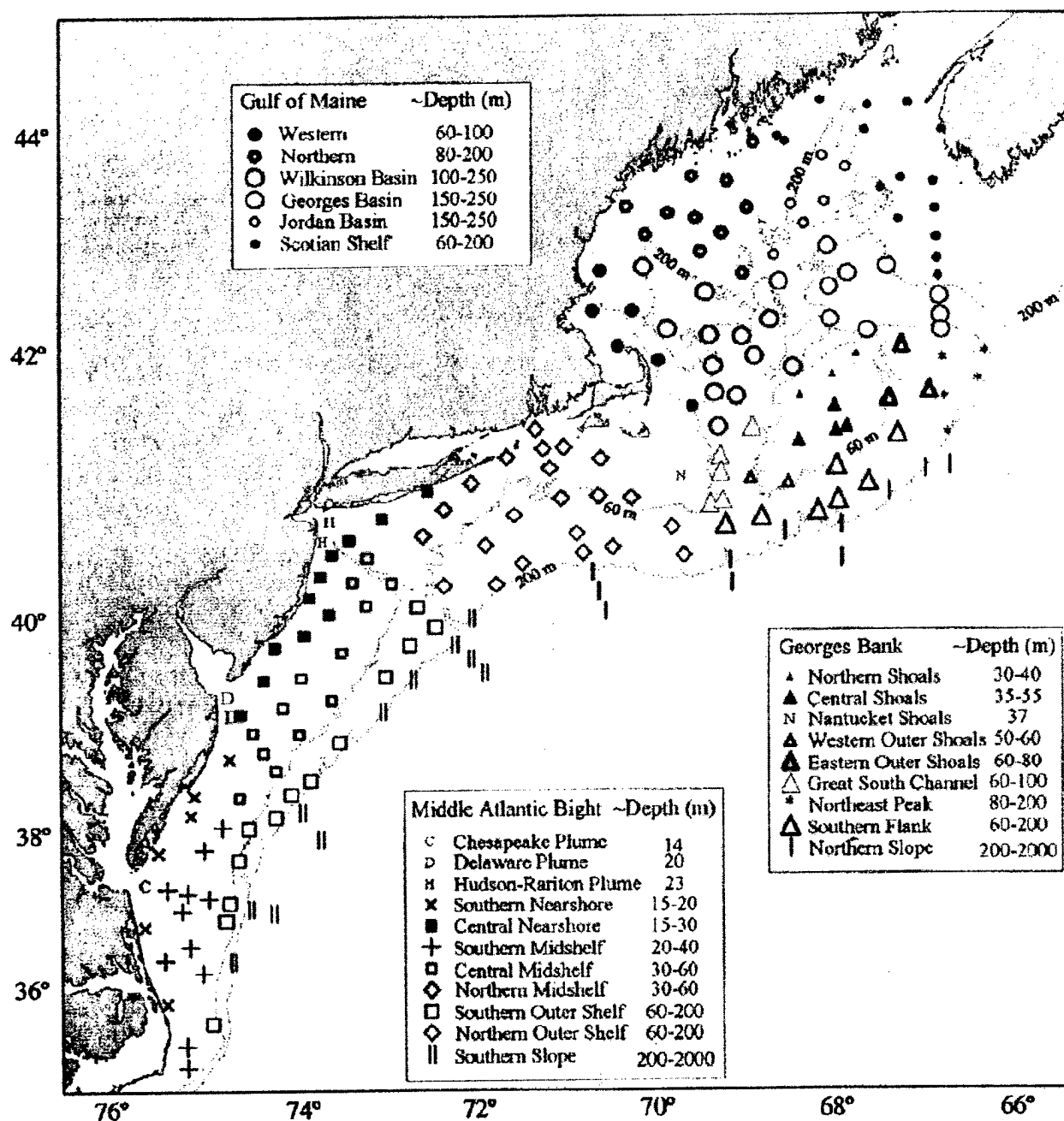
The coefficients α_{X_n} are determined such that the expected value of the sum of the squared errors is minimized. Two different estimates are possible depending on the treatment of the mean value of $\tilde{\theta}_X$.

46

ANOMALY METHOD

Assumptions:

1. zero mean

$$\overline{\tilde{\theta}_X} = 0 \qquad (3.1.3)$$

2. known correlation function

$$\overline{\tilde{\theta}_X \tilde{\theta}_{(X+\delta X)}} = F(\delta X) \qquad (3.1.4)$$

here F is the correlation matrix which is the covariance normalized by the covariance at zero separation. The specific covariance model implemented in this package is:

$$covariance(r) = e^{-r}(1 + r + r^2/3) \qquad (3.1.5)$$

where r is a pseudo-distance calculated as

$$r = \sqrt{\sum_i \frac{(x_i - y_i)^2}{a_i}} \qquad (3.1.6)$$

where

a_i is the local scale factor of the ith independent coordinate,

x_i and y_i are the ith components of x and y respectively.

This pseudo-distance controls the selection of nearest neighbours and the generation of weights.

3. errors are uncorrelated with one another and with the field

$$\overline{\epsilon_m \epsilon_n} = 0 \quad \overline{\epsilon_m \theta_n} = 0 \quad (m \neq n) \qquad (3.1.7)$$

4. known error variance E

$$\overline{\epsilon_m \epsilon_n} = E \quad (m = n) \tag{3.1.8}$$

The optimal linear estimation is:

$$\tilde{\theta}_X = \sum_{n=1}^{num\_closest} C_{Xn}(\sum_m A_{nm}^{-1} \phi_m) \tag{3.1.9}$$

where

$$A_{nm} = \overline{\phi_n \phi_m} = F(X_n - X_m) + E\delta_{nm} \tag{3.1.10}$$

is the covariance matrix and

$$C_{Xn} = \overline{\phi_n \phi_X} = F(X - X_n) \tag{3.1.11}$$

is the covariance vector.

The estimated error variance is

$$\overline{(\theta_X - \tilde{\theta}_X)}^2 = C_{XX} - \sum_{m,n} C_{nX} C_{Xm} A_{nm}^{-1} \tag{3.1.12}$$

The first term is the natural variation in the absence of any data and the second term measures the information provided by the data. Therefore, only the location of the data points, the knowledge of the covariance function and noise level determine the error. The error output in the OAX program is

$$\sqrt{\overline{(\theta_X - \tilde{\theta}_X)}^2} \tag{3.1.13}$$

The noise level E is assigned the same value 0.1 for all the locations in this project.

48

ESTIMATED MEAN METHOD

For our case (actually for general cases) the mean of $\tilde{\theta}_X$ is not known and the ANOMALY METHOD does not apply. A revised estimate is:

$$\hat{\theta}_X = \tilde{\theta} + \sum_n C_{Xn}(\sum_m A_{nm}^{-1}(\phi_m - \tilde{\theta})) \qquad (3.1.14)$$

where $\tilde{\theta}$ is the estimated mean value

$$\tilde{\theta} = \frac{\sum_{m,n} A_{nm}^{-1}\phi_m}{\sum_{m,n} A_{nm}^{-1}} \qquad (3.1.15)$$

The error variance is

$$\overline{(\theta_X - \hat{\theta}_X)}^2 = C_{XX} - \sum_{m,n} C_{nX}A_{nm}^{-1}C_{Xm} + \frac{(1 - \sum_{m,n} C_{Xm}A_{mn}^{-1})^2}{\sum_{m,n} A_{nm}^{-1}} \qquad (3.1.16)$$

The last term is the error associated with the uncertainties of the estimated mean and the first two terms are as already explained in the ANOMALY METHOD. The dimensional errors can be calculated by multiplying the output error by the standard deviation of the dependent variable.

3.2 Results

The resulting estimates of the distribution of Chl_w are illustrated in maps from Figure 3-5 to Figure 3-10 for the six periods: Jan-Feb, Mar-Apr, May-Jun, Jul-Aug, Sep-Oct and Nov-Dec respectively. As defined in the Appendix A, Chl_w is the upper 75 m water column mean of the 11-year (1977-1988) averaged phytoplankton Chlorophyll a concentration. In order to compare with the maps from O'Reilly and Zetlin (1996), we used exactly the same colormaps as they used. The colormap for Chl_w is [0 .125

.25 .5 1 2 4 8] μ/l.
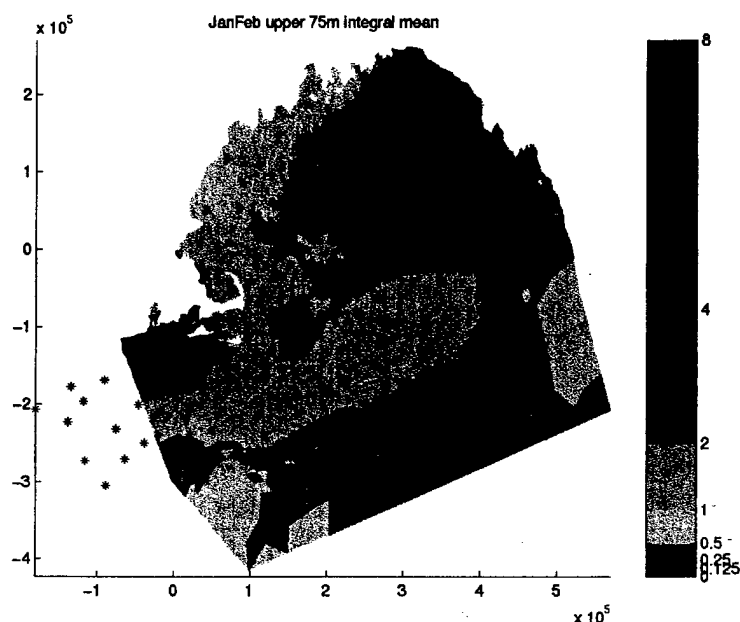
Figure 3-5: Jan-Feb map of Chl_w of default case

3.2.1 Annual cycle of Chl_w

North Middle Atlantic Bight

Since it is relatively deeper on the Northern Outershelf than on the Northern Midshelf, the concentration of Chl_w is generally lower in the former region than in the latter. The highest values of Chl_w during the Jan-Feb period on the North Middle Atlantic Bight are between 2 and 4 μ/l on the Northern Midshelf. As these values are higher than those observed in the preceding period Nov-Dec (which are the minimum ones), the Winter-Spring bloom (WS bloom) has already started on the North Middle Atlantic Bight during the Jan-Feb period. In Mar-Apr, the Chl_w concentration on the North Middle Atlantic Bight reaches its Winter-Spring bloom level $(4-8\mu/l)$. In May-Jun, though in most of the region the bloom level persists, the concentration of

50
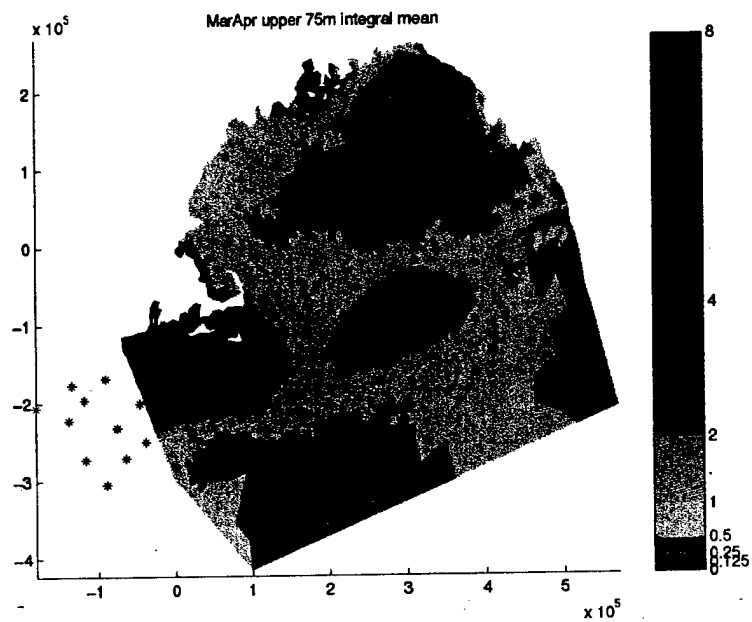
Figure 3-6: Mar-Apr map of Chl_w of default case
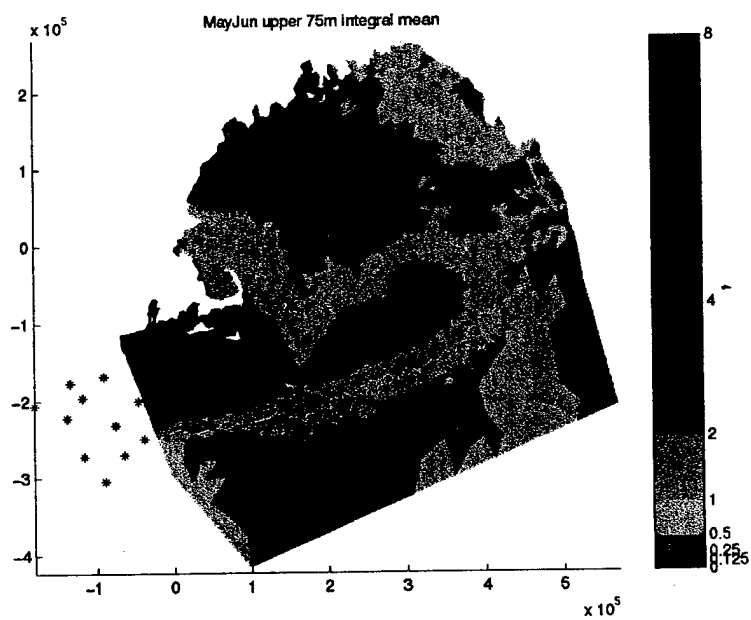
Figure 3-7: May-Jun map of Chl_w of default case

51
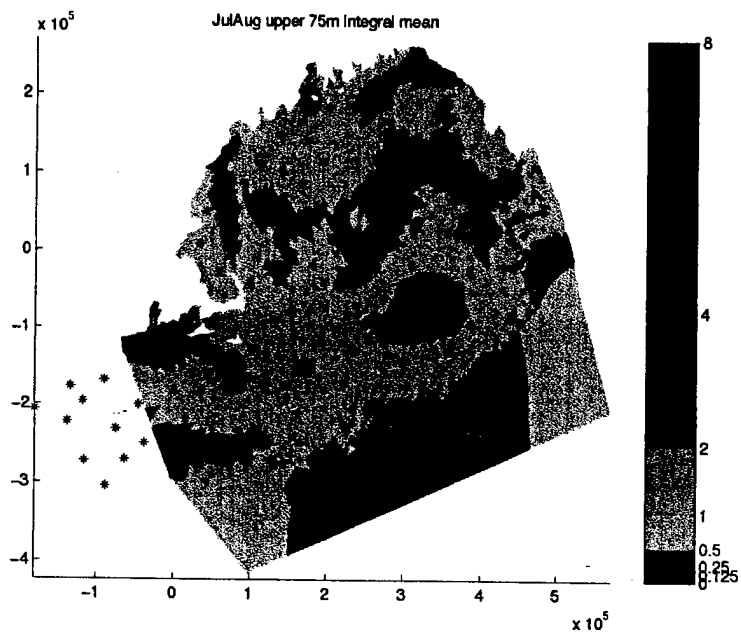
Figure 3-8: Jul-Aug map of Chl_w of default case
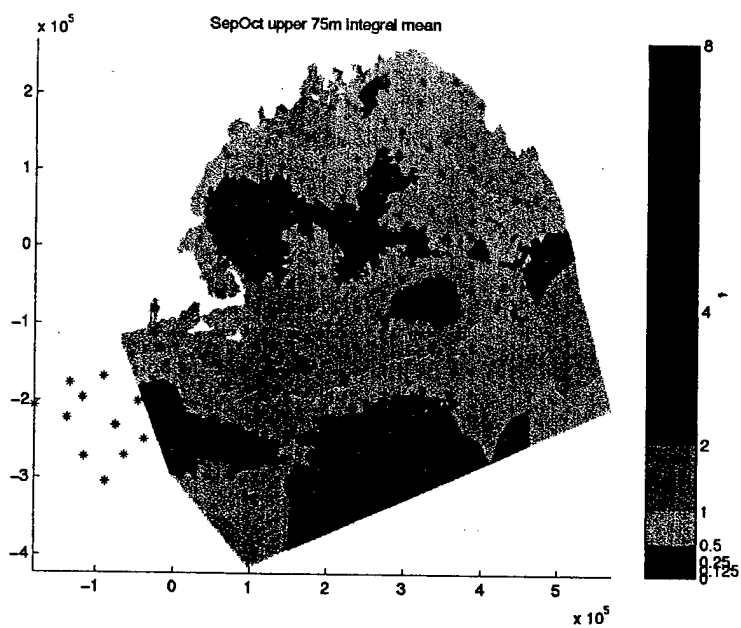
Figure 3-9: Sep-Oct map of Chl_w of default case
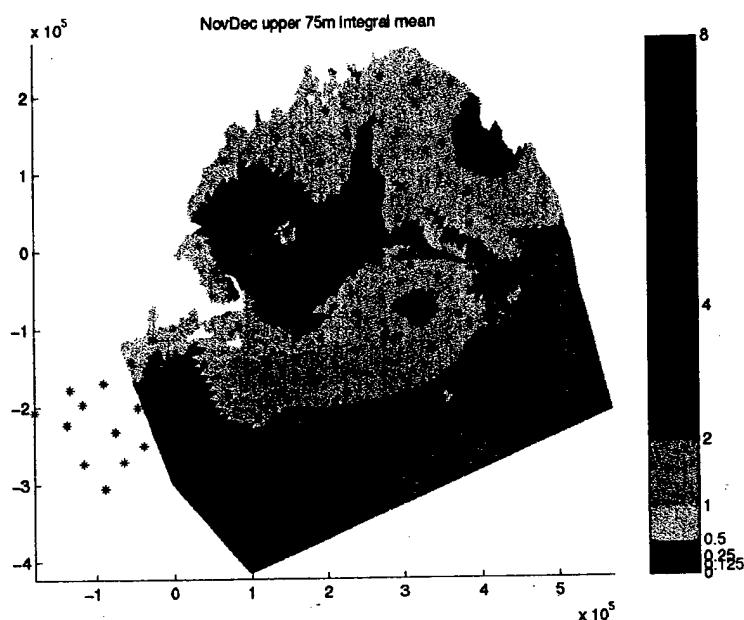
Figure 3-10: Nov-Dec map of Chl$_w$ of default case

Chl$_w$ is generally lower than that of Mar-Apr because the region of maximum bloom, 4 to $8\mu/l$, is smaller. The Chl$_w$ keeps decreasing after the bloom and the rate of decrease is faster in the souththern part of the North Middle Atlantic Bight than in the northern part.

Georges Bank

The contours of Chl$_w$ are approximately parallel to the isobaths with shallower regions such as the Central Shoals and the Northern Shoals (see Fig. 3-3) having higher values than other deeper regions. Since the values of Chl$_w$ on Georges Bank in Jan-Feb are lower than in the preceding Nov-Dec, the Winter-Spring bloom has not yet started on Georges Bank in Jan-Feb. The Winter-Spring bloom starts from March and reaches maximum in April in most of the areas, except in the Great South Channel and on the Northeast Peak where the WS bloom starts later and reaches its maximum during the period of May-Jun. The WS bloom levels are the highest

$(4-8\mu/l)$ in the Central Shoals, the Eastern Outer Shoals and the Nantucket Shoals (see Fig. 3-3). Except in the Nantuchet Shoals and on the Southern Flank the concentration of Chl_w decreases after the WS bloom and the decreasing trend continues until the end of the year. When the Chl_w decreases after the WS bloom, the Chl_w in southern waters decreases faster than that in northern waters. In the Nantucket Shoals after the WS bloom in April, Chl_w reaches its minimum in Jul-Aug and then it increases again to reach another bloom in Sep-Oct. The maximum of Chl_w in Sep-Oct has lower magnitude than that in April and it is called the Fall bloom. On the Southern Flank there appear to be two blooms, the Winter-Spring bloom in May-Jun and the Fall bloom in Sep-Oct, though these two blooms are smaller in magnitude and not very evident. The Winter-Spring bloom starts from Mar-Apr and reaches bloom level in May-Jun. The Fall bloom occurs in Sep-Oct with lower concentration than the Winter-Spring bloom.

Gulf of Maine

The Gulf of Maine, being deeper and located at higher latitudes than the Middle Atlantic Bight and Georges Bank, has lower values of Chl_w than the North Middle Atlantic Bight and Georges Bank throughout the year. The lowest concentrations of Chl_w, less than 0.5 μ/l, occur in a large area of the Georges Basin, Jordan Basin and Scotian Shelf. The nearshore waters of the Western Gulf of Maine, especially the isolated area between Cape Cod and the Penobscot Bay, has generally higher phytoplankton concentration $(2-4\mu/l)$ than the rest of the Gulf of Maine. The Winter-Spring bloom starts here in Jan-Feb. The bloom level occurs in Mar-Apr with larger area of values between 2 and 4 μ/l and the Chl_w values are relatively higher than those of Jan-Feb. The area with values lower than .5 μ/l shrinks from the period Jan-Feb to the period Mar-Apr. In May-Jun, the western Gulf of Maine has lower Chl_w concentrations than in Mar-Apr while the northeastern Gulf of Maine

has values higher than those observed in Mar-Apr. In Jul-Aug, the area with values lower than .5 μ/l of Chl_w in the Gulf of Maine decreases further. The area with values lower than 0.5 μ/l reaches its minimum in the period Sep-Oct. The high values in Nov-Dec near the Scotian Shelf in the northeastern Gulf of Maine are not as reliable since the observations were poor.

3.2.2 Comparision with maps from the monography of O'Reilly and Zetlin (1996)

Our results compare quite well with those of O'Reilly and Zetlin. Our maps (Fig. 3-5 to Fig. 3-10) and their maps (Fig. 3-11) look very similar. The similarities listed below are only some examples.

a. Chl_w contours are parallel to isobaths.

b. The shallower and/or southern regions have relatively higher distributions than the deeper and/or northern regions.

c. The high values 2-4 μ/l of Jan-Feb are in the shallow nearshore waters on the Northern Midshelf of the Middle Atlantic Bight and in the isolated region of the Western Gulf of Maine between Cape Cod and the Penobscot Bay.

d. The Winter-Spring bloom commences earlier in Jan-Feb in the shallow nearshore waters on the North Middle Atlantic Bight and in the isolated region of the Western Gulf of Maine between Cape Cod and the Penobscot Bay, and it commences later in March on Georges Bank.

There are several major differences. Firstly, the minimal Chl_w in O'Reilly and Zetlin's results is during the period of Jul-Aug while according to our results it happens in Sep-Oct. Secondly, there are no estimates around the two islands (Martha's Vineyard and Nantucket) south of Cape Cod in O'Reilly and Zetlin's maps, but the concentration of Chl_w there turns out to be relatively high according to our estima-
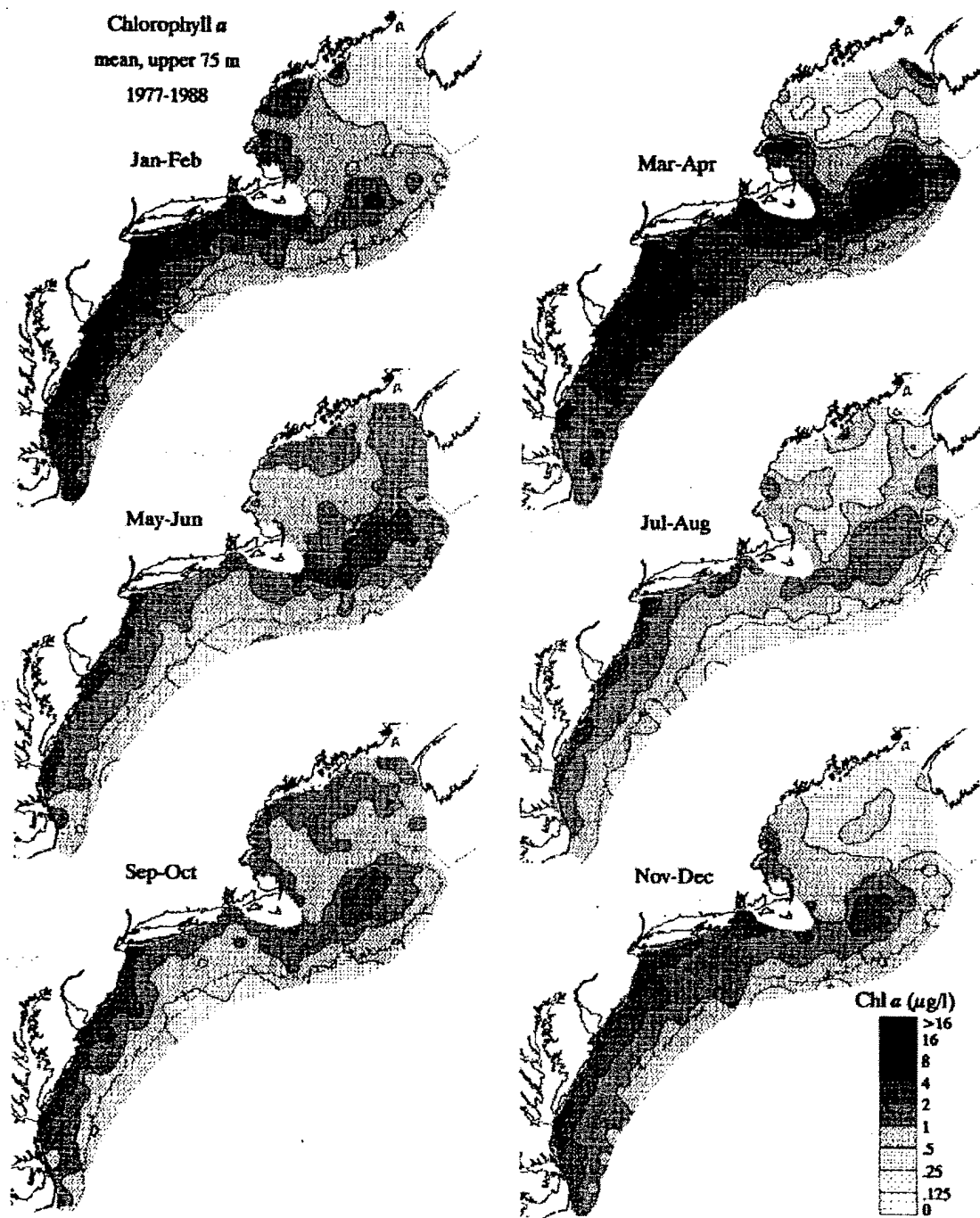
Figure 3-11: Maps of Chl_w (reproduced from O'Reilly and Zetlin, 1996)

tion. Lastly, there are more small scale variations in O'Reilly and Zetlin's contours than in ours. The above discrepancies may depend on the very different approaches we used.

1. Mapping

O'Reilly and Zetlin used Lambert's conic conformal map projection (Uchupi, 1965; Snyder, 1987) to transform from the latitude and longitude coordinates to map coordinates. They used surface III (Sampson, 1988) to generate contoured distributions, and PcxMap supplemented by their own Fortran graphics program to shade and transform the output from Surface III into a PcPaintbrush binary graphics file (Zsoft, 1990). Our mapping approach is very different as detailed in the Appendix A.

2. Estimation

We used correlation as the weight to estimate the grid values while O'Reilly and Zetlin used the inverse square distance ($\frac{1}{distance^2}$). The number of nearest data points we used to estimate a grid value is 50 while they used 8. This is where we think the most significant difference lies. More neighbour data points average out small scale variations and therefore reduce the maximum and increase the minimum.

3.3   Sensitivity tests

We also did sensitivity experiments with regards to the interpolation/extrapolation parameters *num_closest* and *global_scales* and the estimation method based on the Jan-Feb period. *Global_scales* are correlations used in determining the underlying data structure (see Appendix A).

Test A: experiments with *num_closest* which has default value 50.

Case A1: Double *num_closest* (*num_closest* = 100).

Only a slight difference is observed between results of case A1 and the default
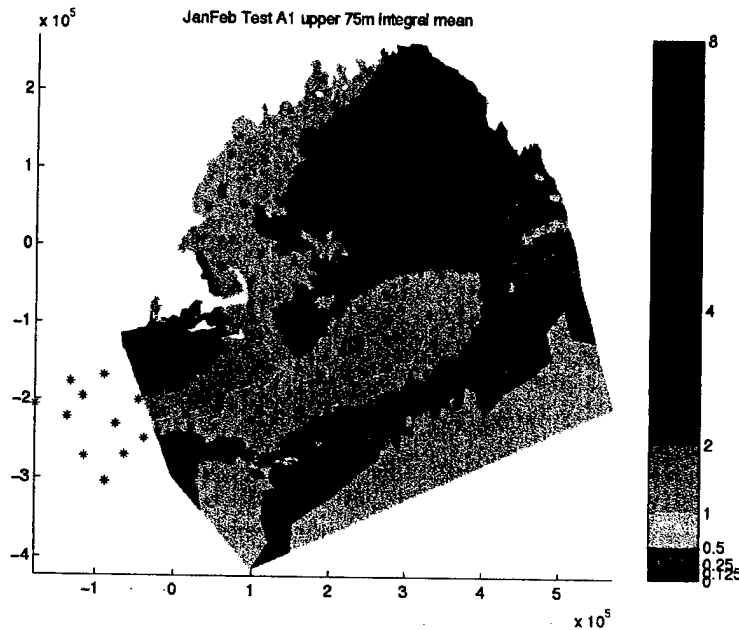
Figure 3-12: Jan-Feb map of Chl_w of case A1

case. In the Chl_w maps, there are fewer small-scale variations in case A1 (Fig. 3-12) than in the default case (Fig. 3-5). Observing the error maps of the default case (Fig. 3-14) and case A1 (Fig. 3-13), we see that the error is slightly smaller in case A1 compared with the default case. For instance, the patch with error values 0.4-0.5 on Georges Bank in case A1 has smaller area than the default case. The area of several patches with relatively high error values in the Gulf of Maine also decreased upon doubling *num_closest*.

Compared with the default case (Chl_w [0.0274 3.3100]; error [0.1937 1.1620]), the variety range of Chl_w decreased ([0.1134 3.2340]) and the error level decreased ([0.1918 1.1320]) as well in Case A1.

Case A2: Half *num_closest* (*num_closest* = 25).

Opposite results to case A1 are obtained. The variety range of Chl_w increased ([0.0714 3.3420]) and the error level increased ([0.1978 1.1990]) as well compared with default case. The Chl_w map and error map of case A2 are shown in Figure 3-15

58
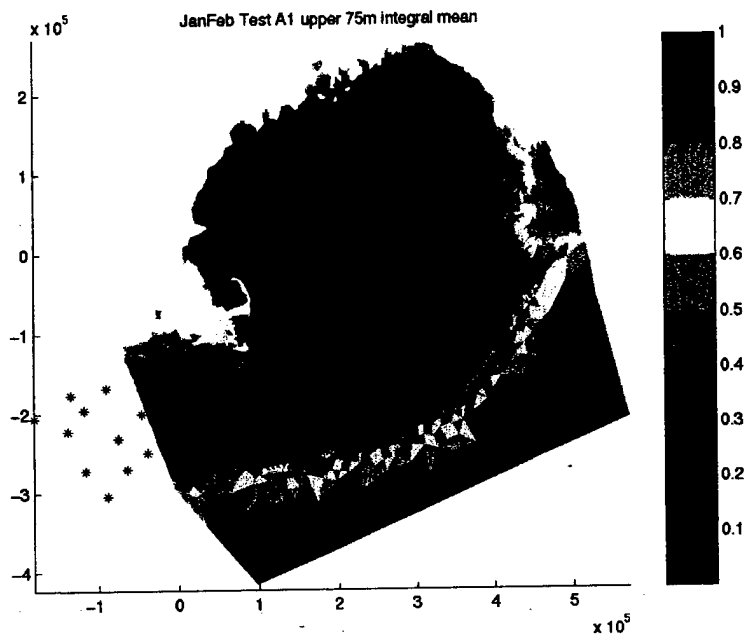
Figure 3-13: Jan-Feb error map of Chl_w of case A1

and Figure 3-16 respectively.

The number of the nearest neighbours is critical for obtaining reliable estimation results. Theoretically, the more the nearest neighbours are the better are the results. Larger number of the nearest neighbours also leads to longer search time. There is not much improvement to the results when the number of the nearest neighbours exceeds a certain value. On the contrary, the increase of *num_closest* could significantly increases the CPU time because of the inversion of a large covariance matrix. The number of the nearest data points is suggested to be any number ranged from 10 to 50 by Charles Hannah et al. (1995). But in our case the differences between case A1, case A2 and the default case are hardly evident in the distribution patterns of Chl_w, so the default value 50 is good enough.

Test B: experiments with *global_scales* **x (cross-isobath) and y (along-isobath) which both have default values 30 km.**
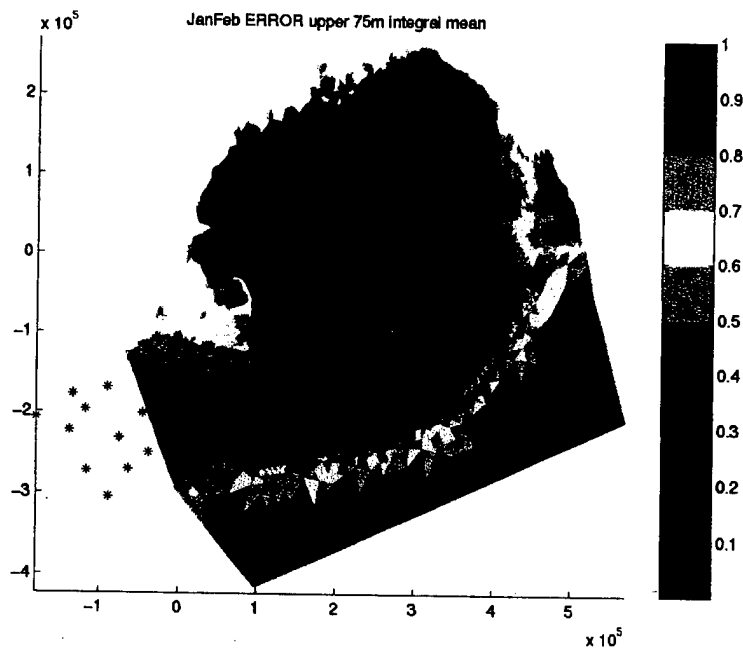
Figure 3-14: Jan-Feb error map of Chl_w of default case

Case B1: Simultaneously double x and y $(x = y = 60km)$.

For this experiment the Chl_w and error maps are basically the same as the default case. The only difference is that case B1 has a slightly smaller minimum of error than the defaulf case.

Case B2: Simutaneously tenth x and y $(x = y = 3km)$.

Case B3: Double x $(x = 60km)$ and tenth y $(y = 3km)$.

Case B4: Tenth x $(x = 3km)$ and double y $(y = 60km)$.

The results of this series of experiments are very similar. The test B suggests that the *global_scales* (x and y) may have a little affect on the error level but not on the estimation results. The figures of these cases are not attached as they are little different from the default case.

The *global_scales* for time and depth will not affect the estimation results significantly since we integrated Chlorophyll *a* vertically in the water column and we also
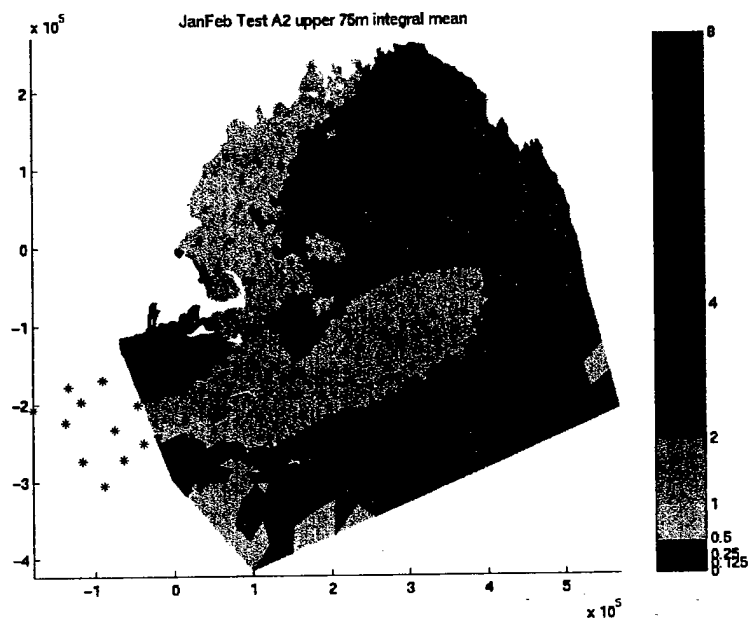
Figure 3-15: Jan-Feb map of Chl_w of case A2
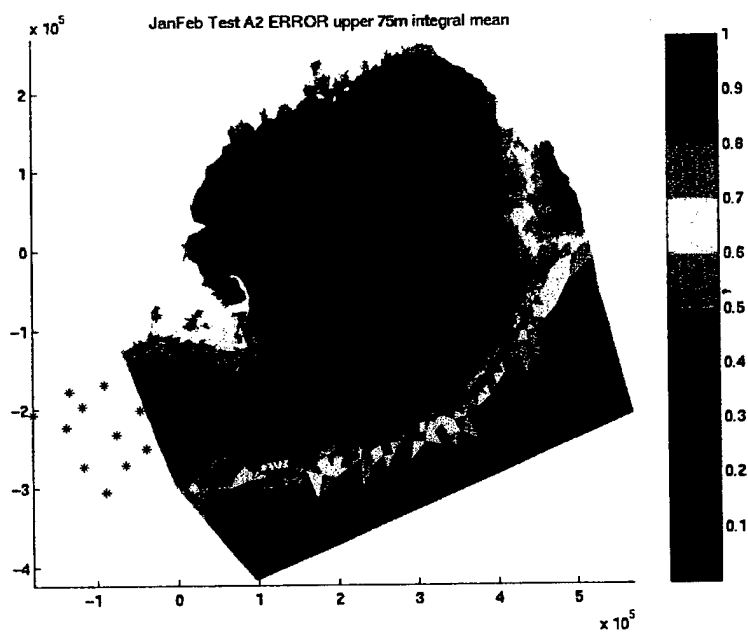
Figure 3-16: Jan-Feb error map of Chl_w of case A2

separated the data into six two-month periods.

Test C: optimal interpolation with the ANOMALY METHOD.

The mean of Chlorophyll a is substracted first to get the anomaly data and the anomaly data is fed into OAX5 for interpolation. Then the mean value is added back to the results. Since the mean of Chlorophyll a is about 1.02 μ/l, the distribution of Chl_w of this experiment is always and everywhere higher than 1 μ/l, which is not reasonable. This verifies that for our case the ESTIMATED MEAN METHOD should be used instead of the ANOMALY METHOD.

Chapter 4

An adjoint data assimilation approach to diagnosis of physical and biological controls on phytoplankton in the Gulf of Maine - Georges Bank region

4.1 Methods

4.1.1 Circulation field

The circulation field of the Gulf of Maine-Georges Bank region is depicted in Figure 4-1 (Beardsley et al., 1997). The general circulation in the Gulf of Maine is cyclonic (Biglow, 1927; Beardsley et al., 1997) and that on Georges Bank is anticyclonic. There are two primary and distinct inflows into this region, one is the Scotian Shelf

fresh water through the Northern Channel (north of Browns Bank), another one is the slope water through the Northeast Channel. Other minor sources are St. John River, St. Croix River, Penobscot River etc.. Outflows go to the west mainly along the 60 m and 100 m isobaths south of Georges Bank and the Nantucket Shoals. The inflow from the Scotian Shelf continues past the mouth of the Bay of Fundy and joins the Maine Coastal Current, together with the input from the St. John River and other sources. The Maine Coastal Current separates into two branches near Penobscot Bay, with one branch flowing seawards and feeding the Jordan Basin cyclonic gyre. The other branch continues along the coast and bifurcates when it gets to Cape Cod, with a portion branching seawards and joining the clockwise circulation on Georges Bank and another branch continuing southwards, before turning westward and joining the outflow along the 60 m isobath. Before the bifurcation at Cape Cod, a subbranch feeds into the circulation of Massachusetts Bay and Cape Cod Bay from the point of Cape Ann. The Great South Channel (sill depth 70 m), the Northeast Channel (sill depth 230 m), and the Northern Channel (140 m) connect the Gulf with the adjacent waters on the continental slope. Exchange of seawater between the Gulf and North Atlantic is fairly restricted, occuring mostly through the deep Northeast Channel (Ramp et al., 1985; Mountain and Jessen, 1987).

Intense modeling activities have been carried out in the Gulf of Maine-Georges Bank region. Lynch et al. (1996) employed a finite element approach to facilitate realistic representation of the complex geometry in this area. The model is three-dimensional, hydrostatic, fully nonlinear and it incorporates a level 2.5 turbulence closure scheme (Mellor and Yamada, 1982) to represent the vertical mixing of momentum, heat and mass. The climatological mean circulation has been shown to compare well with available observations (Naimie, 1996; Lynch et al., 1997). The solutions are separated into six bi-monthly periods and are the inputs to the two-dimensional ADR (advection-diffusion-reaction) equation on the same grid. Boundary conditions used
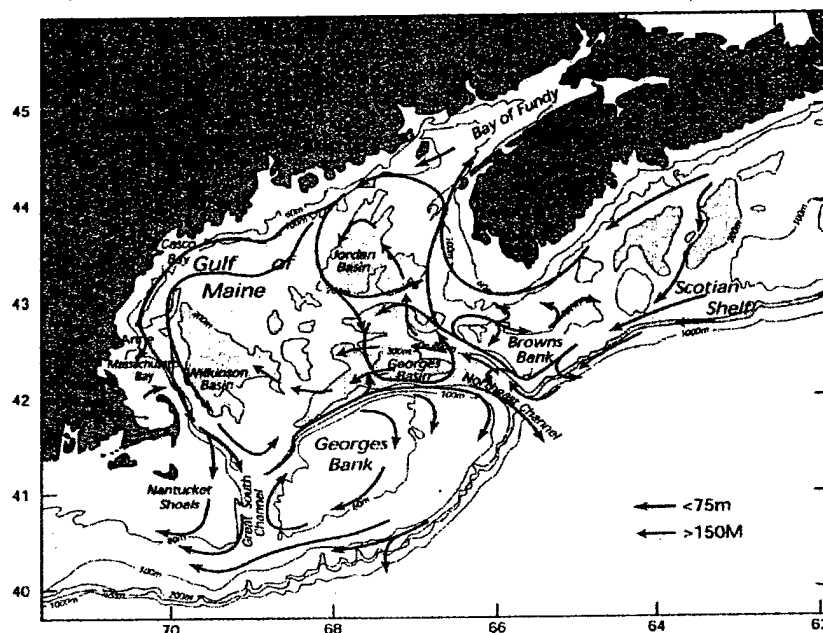
Figure 4-1: The general circulation in the Gulf of Maine during stratified season (Beardsley et al., 1997). This picture is reproduced from McGillicuddy et al., 1998).

to solve the ADR equation are (1) no flux through solid boundaries, (2) specified concentration at the inflow, and (3) the concentration at the outflow is computed assuming no diffusion.

4.1.2 An adjoint data assimilation technique

Data assimilation techniques have been successfully applied in meteorology and are routinely used with operational weather forcast models. More recently, theses techniques have been used with physical oceanographic circulation models. Reviews of data assimilation methods as applied in meteorology and oceanography are found in Bengtsson et al. (1981), Lorenc (1986), Haidvogel and Robinson (1989), and Ghil and Malanotte-Rizzoli (1991). In the field of biological oceanography where satellite systems and other continuously-recording instruments are providing large quantities

of data (Dickey, 1991) and mathematical models are frequently used, data assimilation is becoming an important topic. There exists a variety of assimilation techniques including successive correction (Cressman, 1959; Bratseth, 1986), optimal interpolation (Gandin, 1963; Lorenc, 1981), Kalman filtering (Kalman, 1960; Kalman and Bucy, 1961; Ghil et al., 1981) and the variational method (Lewis and Derber, 1985; Derber, 1985; Le Dimet and Talagrand, 1986; Lorenc, 1988 a, b). The data assimilation technique used in this study is the variational, or adjoint method. The adjoint method has been used for parameter estimation in a variety of oceanographic systems (Panchang and O'Brien, 1989; Lardner and Das, 1994). More recently, it has been used with simple biological models (Lawson et al., 1995). In the model (McGillicuddy et al., 1998) we use, the computer code for the adjoint is constructed directly from the model computer code. This technique is straightforward and reduces the chance of introducing errors in the construction of the adjoint code.

The coupled model we use to study our problem is from McGillicuddy et al. (1998). The two-dimensional advection-diffusion-reaction equation for the positive definite depth-averaged biology concentration $B(x, y, t)$ is expressed as:

$$\frac{\partial B}{\partial t} + \vec{v} \cdot \nabla B - \frac{1}{H} \nabla \cdot (HK\nabla B) = R(x, y) \qquad (4.1.1)$$

where H is the bottom depth. The reaction term $R(x, y)$ varies in space only, and serves as a highly idealized parameterization of population dynamics. Positive R implies net growth and negative R implies net mortality.

In order to measure the misfit between predicted B and observed concentration B_{obs}, a cost function J is defined:

$$J = \int_{-L_x}^{L_x} \int_{-L_y}^{L_y} \int_{t_0}^{t_1} \delta_M (B - B_{obs})^2 dx dy dt \qquad (4.1.2)$$

66

where L_x and L_y represent the extent of the horizontal domain of interest, and δ_M has value of one wherever observation is available in space and time, and zero otherwise.

Given initial conditions $B_{obs}(x, y, t_o)$, the output from the fprward model is the value of the cost function, which gives a measure of the misfit between the model-derived concentration B and the measured $B_{obs}(x, y, t_1)$ when the next set of observation is available at t_1. Integration of the adjoint equation then transforms these measures of misfit into the gradient of the cost function with respect to the control variable (in thsi case, R). The gradient is then used to find the direction in which the value of R is adjusted in order to decrease the difference between the model output and the data. However, the cost function is typically not expressed explicitly in terms of R and in order to avoid the difficulty of the gradient calculation, Lagrange multipliers are introduced and the Lagrange function, L, is defined as

$$L = J + \int_{-L_x}^{L_x} \int_{-L_y}^{L_y} \int_{t_0}^{t_1} \lambda \left(\frac{\partial B}{\partial t} + \vec{v} \cdot \nabla B - \frac{1}{H} \nabla \cdot (HK\nabla B) - R \right) dx\,dy\,dt \qquad (4.1.3)$$

where $\lambda = \lambda(x, y, t)$ is the unknown Lagrange multiplier.

The model equations, the adjoint equations and the gradient of the cost function are obtained by finding a saddle point of the Lagrange function, that is, a point in B, R, λ space where the partial derivatives of L vanish simultaneously, $\frac{\partial L}{\partial B} = \frac{\partial L}{\partial R} = \frac{\partial L}{\partial \lambda} = 0$. The R that minimizes L at the saddle point is to be obtained. The requirement of $\frac{\partial L}{\partial \lambda} = 0$ returns the model equation. The adjoint model is an advection-diffusion-reaction equation for the Lagrange multiplier forced by the misfit between the modeled and observed values of B

$$-\frac{\partial \lambda}{\partial t} - \nabla \cdot \lambda \vec{v} - \frac{1}{H} \nabla \cdot (HK\nabla \lambda) = -2\delta_M (B - B_{obs}) \qquad (4.1.4)$$

with homogeneous boundary conditions.

The gradient of the cost function with respect to the control variable R can also be derived through the integration of the adjoint model

$$\frac{\partial J}{\partial R} = \int_{t_0}^{t_1} \lambda(x, y, t) dt \qquad (4.1.5)$$

Once the direction to adjust R is found, the step size, that is the size of the change in that particular direction, must be determined. After the variables are adjusted by the calculated step size and direction, the model is again applied and the process repeated. Hence, by repeating the iterative procedure which includes a model run, an adjoint run and a step size calculation, convergence is reached on the values of $R(x, y)$ that minimize the cost function. This also provides the best fit of B to the observation B_{obs} under the constraint that the forward model equation is satisfied. The optimal stepsize is determined using the steepest descent method as in Derber (1985).

4.2 Results

The interpretation of the effect of the circulation on passively drifting biology is confined to the region which is not affected by the boundary effects, since the distribution of phytoplankton is not very well sampled in some of the inflow regions as shown in chapter 3. For this purpose, McGillicuddy et al. (1998) carried out a series of control volume simulations. In the experiments, the concentration is assigned with value one uniformly in the domain and zero at inflow. After two months of forward integration for each of the six bi-monthly periods, a substantial region of the domain not affected by boundary effects is found, although the details are slightly different for different periods. The "region of interest" as defined in McGilicuddy et al. (1998) is

the intersection of the areas in which (1) observations are available and (2) boundary effects are minimal on bi-monthly time scales (Fig. 4-2, McGillicuddy et al., 1998). Our study will be confined inside of the "region of interest".

As we see in Figure 4-1, there are flows onto and away from Georges Bank. The questions of interest are where the transport pathways are and how much the circulation retains the population on the Bank under the influence of the flows. Therefore, a second set of control volume two-month integrations were performed in McGillicuddy et al. (1998) for each of the bi-monthly periods, with the initial conditions set to one on the Bank and zero elsewhere (Fig. 4-3 (a)). The initial conditons and integration results for periods January-February, May-June and September-October are illustrated in Figure 4-3 (McGillicuddy et al., 1998). In the period of January-February (Fig. 4-3 (b)) the high concentration on Georges Bank is diluted by the zero-concentration inflow from the Gulf of Maine. A pathway to the southwest brings the high concentration from the crest of the Bank to the Great South Channel and continues to the west until it is out of the domain. The concentration center is shifted to the southwest edge from the center of the Bank. During spring time (Fig. 4-3 (c)) the dilution caused by the inflow from the Gulf of Maine and the southwestward transport from the Bank crest still exist, however the established seasonal stratification enables the clockwise circulation to be more retentive. Although the concentration center is shifted a little bit to the west on the Bank, the organisms are mostly confined inside of the 60 m isobath and the concentration in the Great South Channel is lower than its winter values. The influence of the southwestward flow off the Bank crest is still evident, but the concentration center is moved to the west instead of southwest, which serves as another piece of evidence for the more retentive clockwise flow pattern on the Bank. When the seasonal stratification is the strongest during summer time, the retentive character of the Georges Bank circulation system reaches its peak (Fig. 4-3). The distribution remains centered on the Bank as in the initial condition and
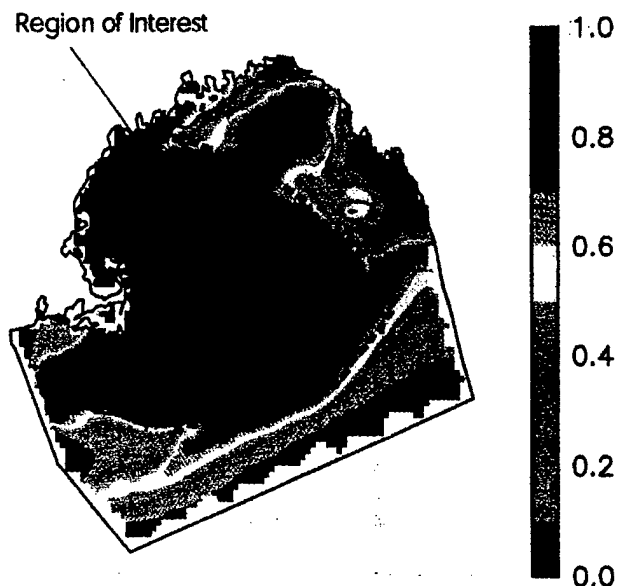
Figure 4-2: The first set of control volume experiment (reproduced from McGillicuddy et al., 1998) which defines the "region of interest".

the flow drifting to the northwest has a very low concentration of organism.

The inversion work is separated into six bi-monthly cases. In each assimilation experiment, initial conditions are specified, and $R(x, y)$ is sought in order for the forward model integration to fit the data of the next period. For example, for the first period from January-February to March-April, the initial condition is the observation from January-February, and $R(x, y)$ is sought in order for the forward model integration to fit the observation of March-April. The inversion results after the cost function values are reduced approximately an order of magnitude are illustrated in six figures from Figure 4-4 to Figure 4-9, with each figure representing each of the six periods: January-February to March-April, March-April to May-June, May-June to July-August, July-August to September-October, September-October to November-December, and November-December to January-February. The observations are plotted again in the top row of each figure with a colorbar [0 0.125 0.25 0.5 1 1.5 2 2.5 3
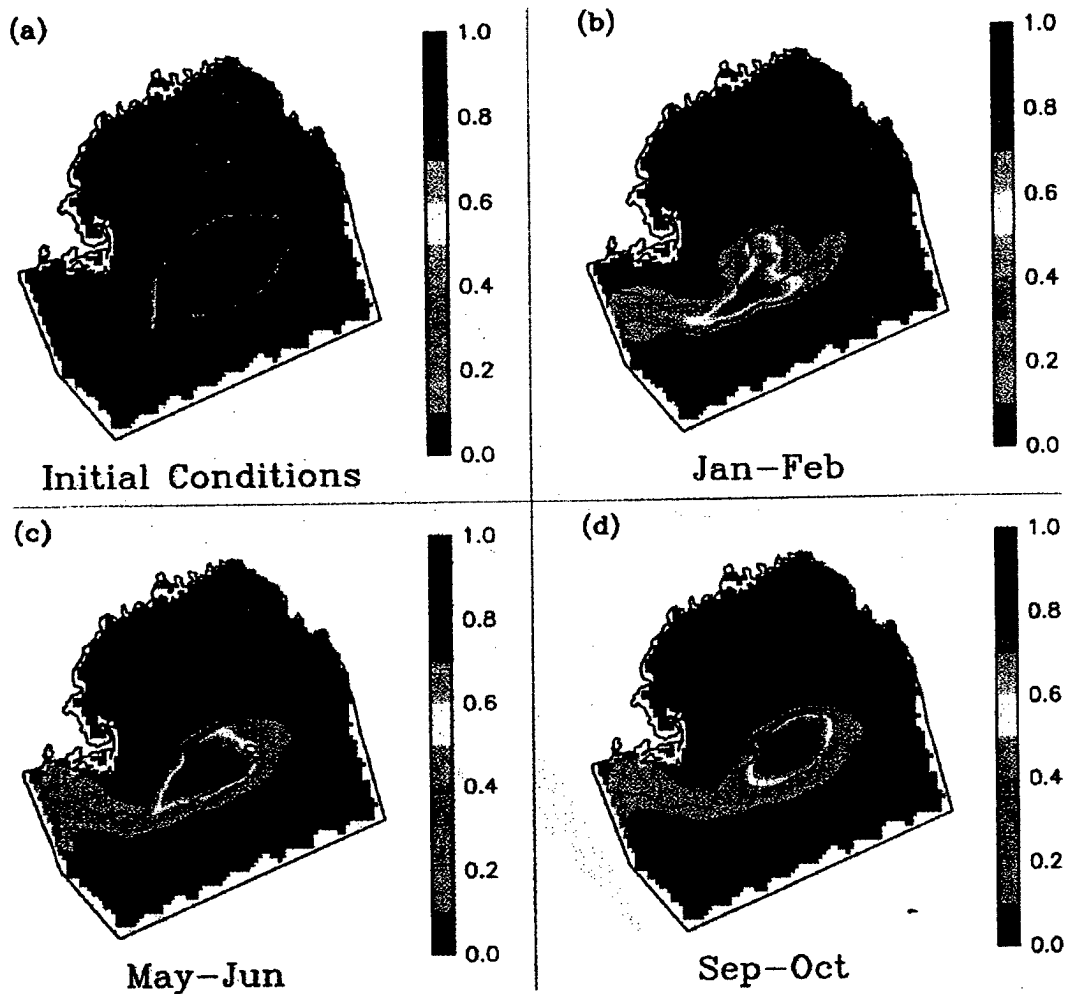
Figure 4-3: The second set of control volume experiment (reproduced from McGillicuddy et al., 1998): initial conditions (a) and the results after two months of integration using the flow field of period Jan-Feb (b), May-Jun (c), and Sep-Oct (d).

71

3.5 4 8] μ/l finer than in Chapter 3 for the convenience in analysing the inversion re-
sults. The inversion results are maps of the source term, the advective flux divergence
term, the diffusive flux divergence term and the tendency term in the ADR equation.
The tendency term is calculated as the sum of the other three terms. The modeled
concentrations of the last forward model run all very much resemble the correspond-
ing observations and so only that from the first period which is initialized with the
January-February observation is shown in Figure 4-10 as an example to be compared
with the March-April data of Figure 4-4 and 4-5. The cost function values are re-
duced approximately an order of magnitude after 50 iterations with the exception of
the periods from July-August to September-October and from September-October to
November-December (Fig. 4-11). In these last two periods, the cost function values
are reduced approximately an order of magnitude after 200 iterations.

January-February to March-April

The source term map shows strong growth (red shading) on the crest of Georges
Bank, moderate growth (yellow shading) in the coastal area of Massachusetts Bay
and weak growth (green shading) in most of the area of the Gulf of Maine, especially
in the western Gulf. On Georges Bank, a balance exists between the advection and
the source term. Flow onto the crest across the northern flank of the Bank imports
low concentrations of phytoplankton from the Gulf of Maine. The positive advec-
tive flux divergence on the southern part of the Bank transports high concentration
fluid from the crest towards the Great South Channel on the southwest (see Fig.
4(b), McGillicuddy et al., 1998). However, the net growth and net mortality coincide
with the negative and positive advective flux divergence in space, respectively. The
net growth has larger magnitude than the negative advective flux divergence and
the net mortality has smaller magnitude than the positive advective flux divergence,
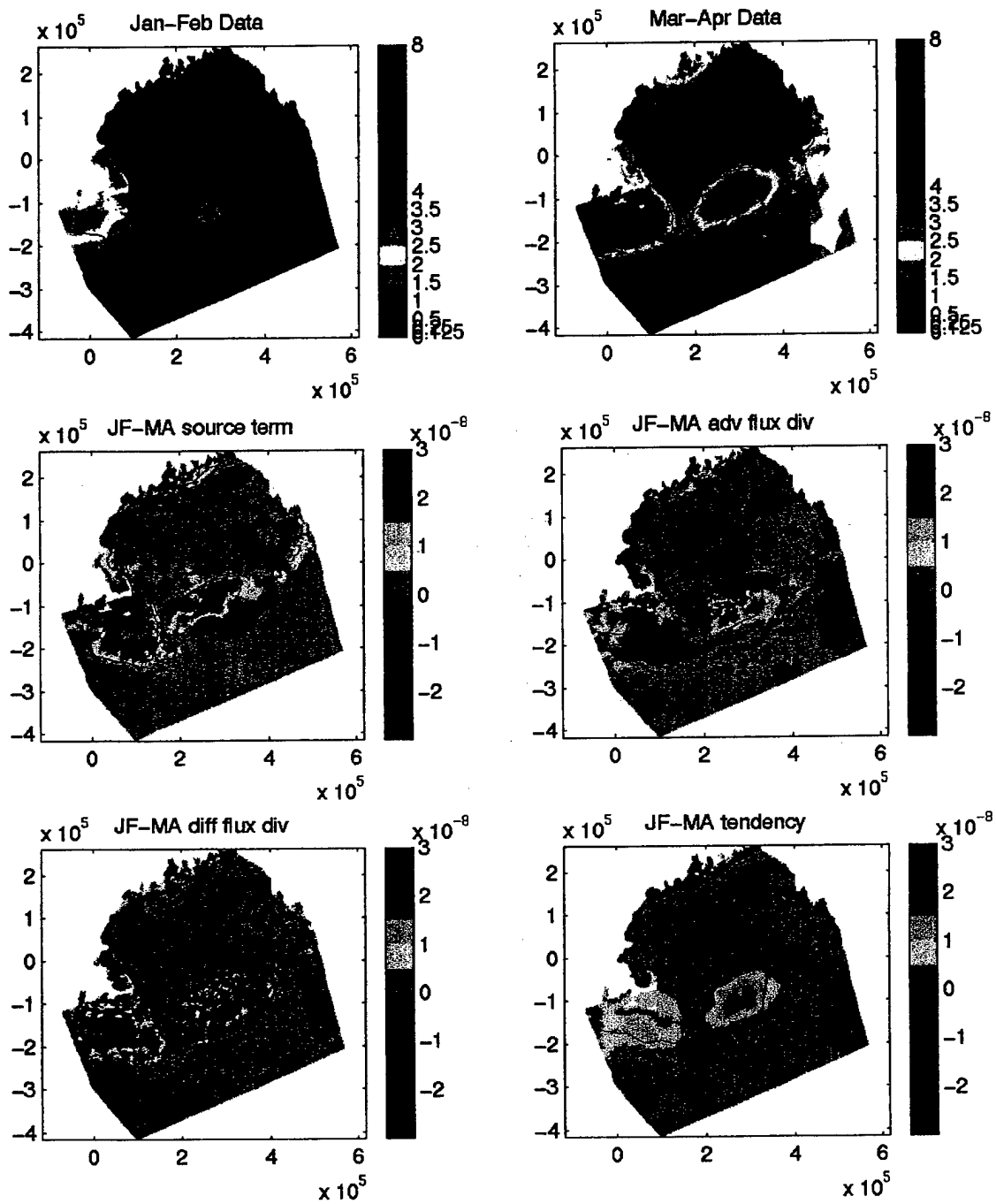therefore the overall tendency on Georges Bank is for the concentration to increase

Figure 4-4: The inversion results for the period from Jan-Feb to Mar-Apr.

from January-February to March-April. In the coastal region of Massachusetts Bay, the negative contribution from advection is weaker than that from the net moderate growth. The tendency is then largely controlled by the net moderate growth. The concentration in this region increases slightly. In the Gulf of Maine, the tendency of phytoplankton varies with space. Only some regions in the interior of the Gulf and the western coast have positive tendencies.

March-April to May-June

In the coastal region of Cape Ann and Massachusetts Bay, the positive source term has greater magnitude than in the previous period. However, strong negative divergence of advective flux brings low-concentration water here from the interior of the Gulf of Maine. The net tendency of this region is that concentration decreases from March-April to May-June, with the negative contribution from the advective flux divergence overshadowing the growth. On Georges Bank, compared with the previous period, the source term decreases with smaller positive values in the center and the northern part of the Bank. Due to the stronger stratification (compared with the previous period), the clockwise flow pattern on the Bank is more retentive. The position of the dipole structure of advective flux divergence (red and blue) on the Bank rotates slightly clockwise and the negative contribution from the Gulf of Maine decreases in magnitude. The combined influence on Georges Bank is that the concentration over most of the region decreases, except for a small area of the western Bank where the concentration increases a little bit. In the Gulf of Maine, the tendency is negative and relatively small.

May-June to July-August

In the coastal region of Cape Ann, Masschusetts Bay and Cape Cod Bay, the magnitude of net growth is smaller than that from March-April to May-June. Because
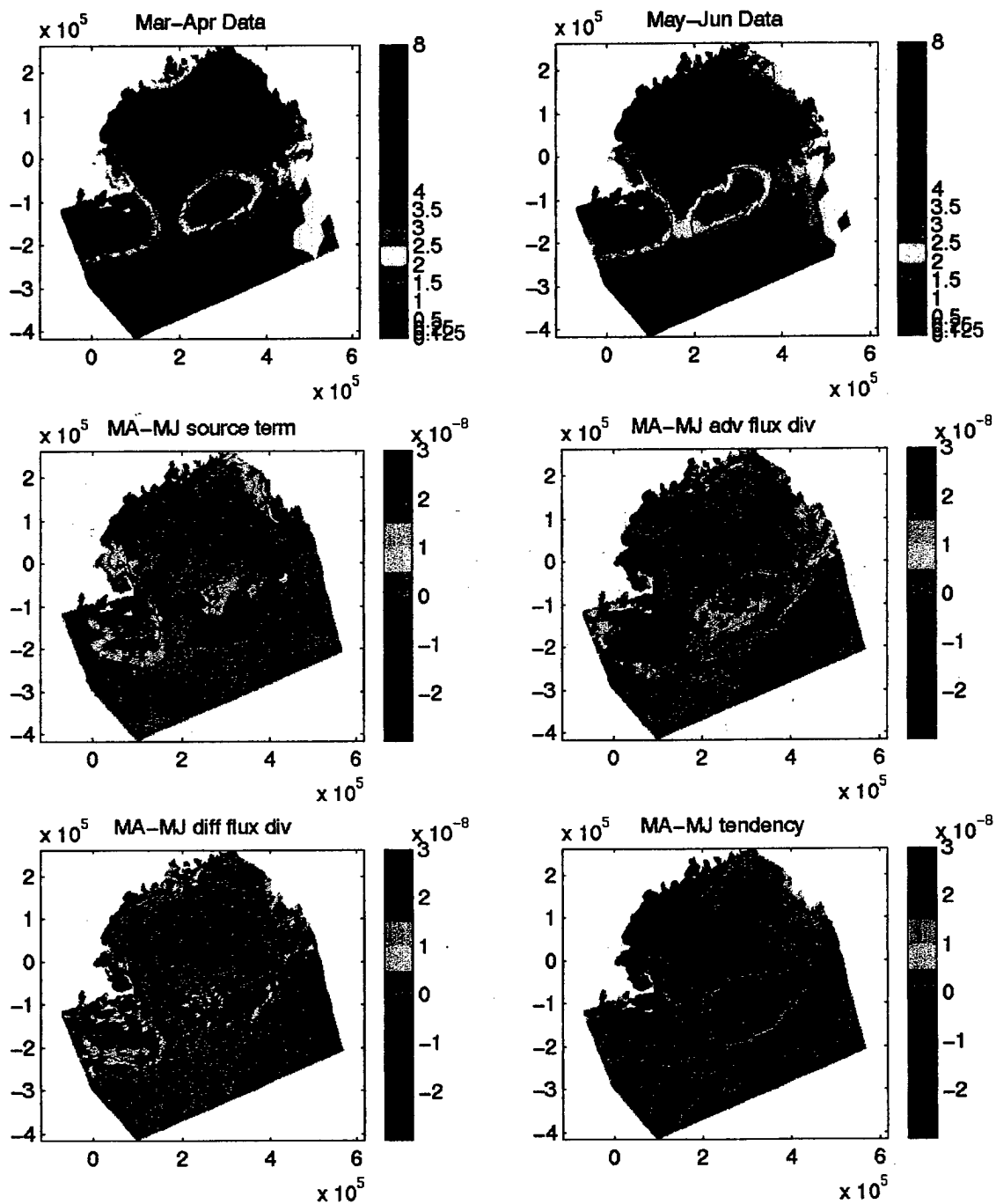
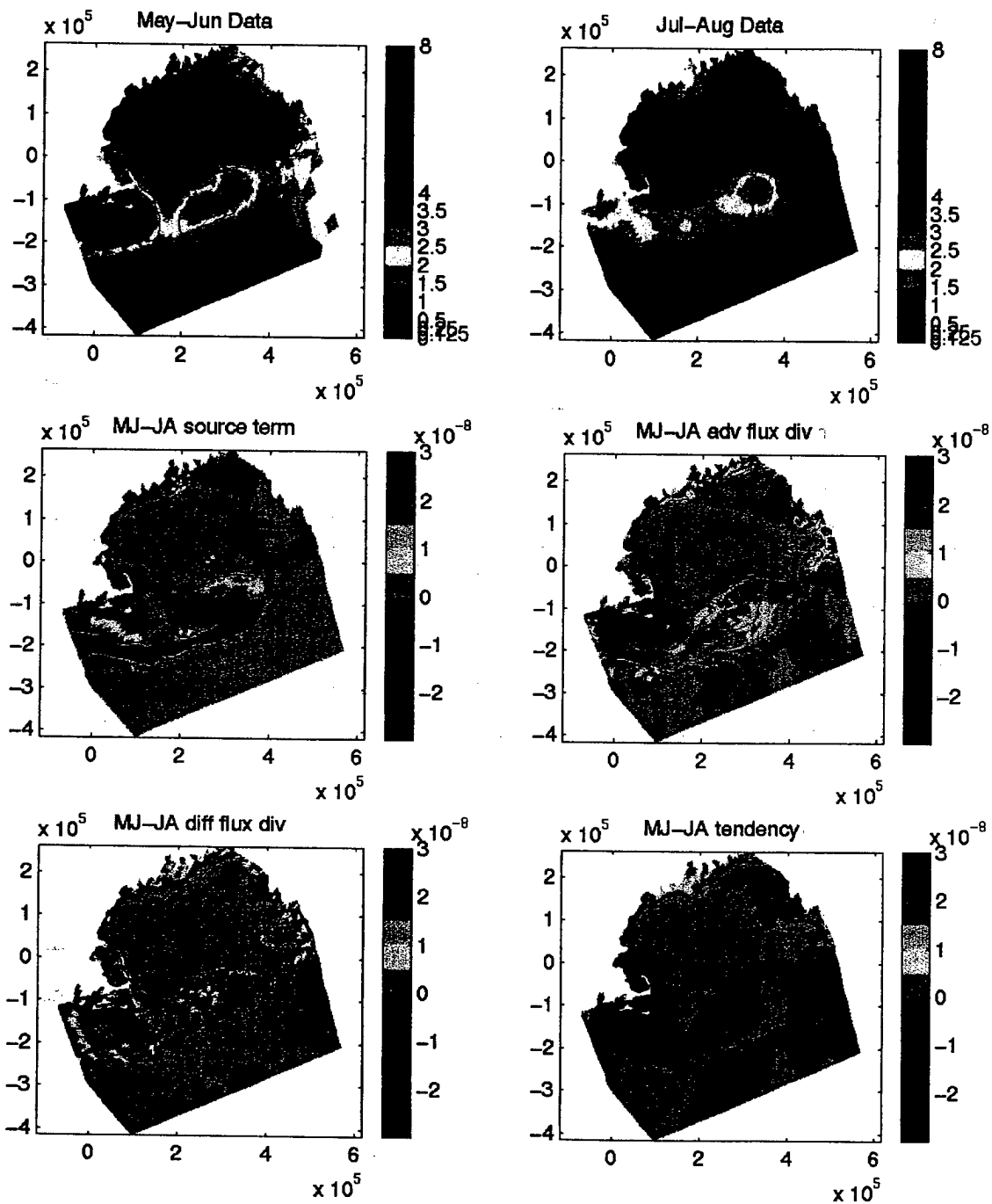Figure 4-5: The inversion results for the period from Mar-Apr to May-Jun.

Figure 4-6: The inversion results for the period from May-Jun to Jul-Aug.

the flow field still brings low concentration from the Gulf of Maine into this region and this influence overweighs the weak growth, the overall tendency of this region is negative and has a magnitude similar to the previous period. On Georges Bank, the dipole structure of the advective flux divergence rotates clockwise further and the magnitudes are smaller than that in the preceding period. On Georges Bank, the source term has negative contribution except in a small region on the northeastern edge. With the small area of net growth overshadowed by the negative advective flux divergence from the Gulf and the net mortality exceeding the positive advective flux divergence from the crest to the Great South Channel, the concentration in the whole region of Georges Bank has a tendency to decrease. Except in the coastal region of Cape Ann, Massachusetts Bay and Cape Cod Bay, the tendency in the Gulf of Maine is for the concentration to increase slightly.

July-August to September-October

On Georges Bank, the source term and the advective flux divergence term mirror each other in space almost exactly. On the southern and northern Bank, the source term is positive and the advection term is negative. On the eastern and western Bank, the source term is negative and the advection term is positive. Except in a small area on the northern and southern edge, the tendency is to decrease with the net mortality overcoming the positive advection and the net growth overcome by the negative advection. On the southern and northern edge, there is small-area very weak increase. In the Gulf of Maine, the situation in the western coast does not change much from the previous period. Inside of the Gulf of Maine the tendency of increase from May-June to July-August is substituted by a trend that is partial increase and partial decline, with the western part having more tendency to decrease and the eastern part having more tendency to increase. The increase and decrease are both very weak.
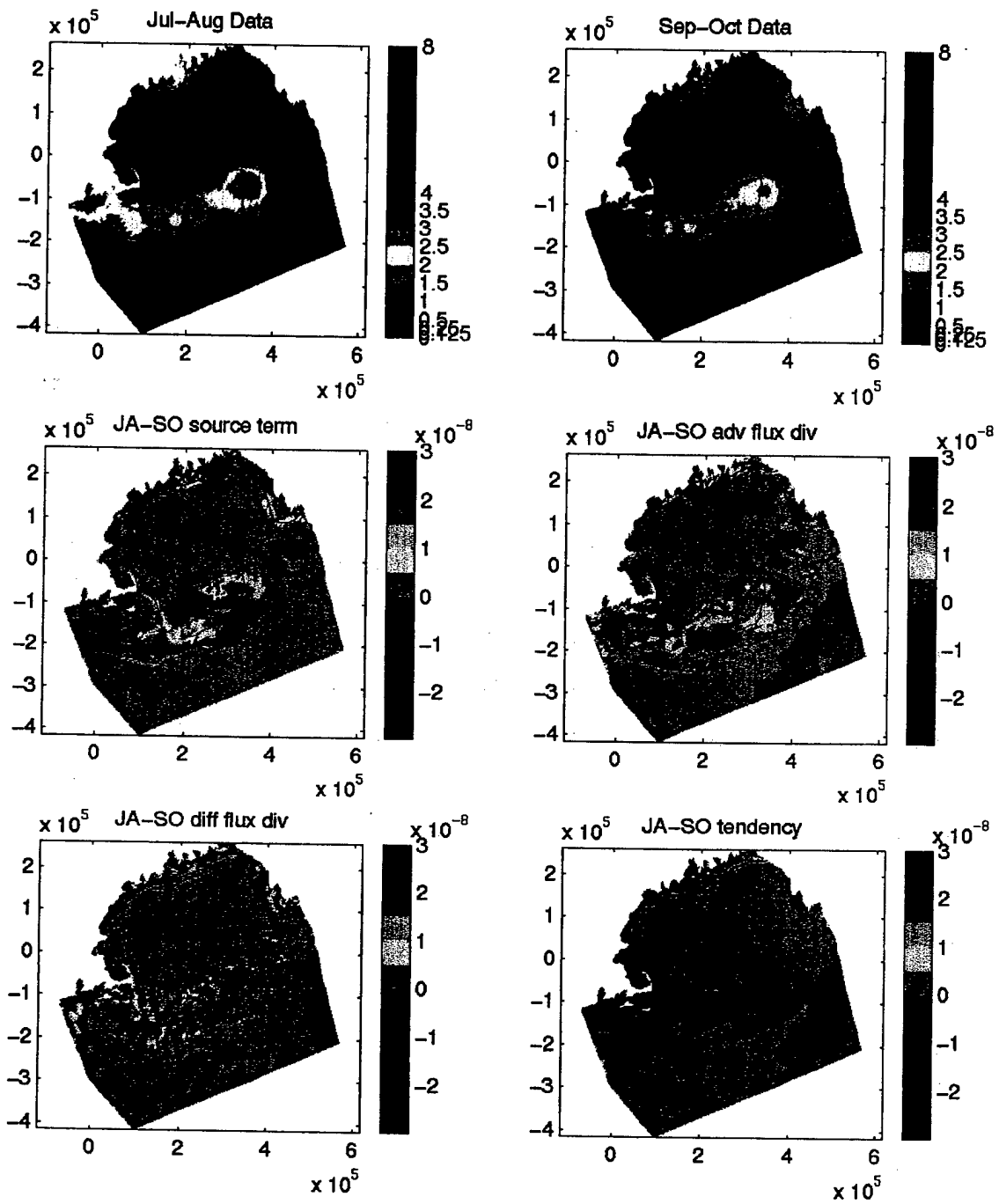
Figure 4-7: The inversion results for the period from Jul-Aug to Sep-Oct.

September-October to November-December

The source term shows moderate growth on northern and northeastern Georges Bank and net mortality on rest of the Bank. Although the strong seasonal stratification in summer time from September-October enables Georges Bank to be sort of resistant to the influence from the Gulf of Maine, the negative advective flux divergence contribution to the Bank still persists on the north flank. The dipole structure of advective flux divergence on the Bank is not shifted clockwise as much as in the preceding period, which suggests that the circulation on the Bank is not so retentive as in the preceding period. On the northern Bank, the net growth is overshadowed by the low concentration inflow from the Gulf of Maine or from the western part of the Bank and the tendency is for the concentration to decrease. On the southern Bank, there is a region where the positive concentration input from the Bank crest counteracts the mortality and the tendency is slightly positive. In rest of the area on the Bank, the net mortality has a larger magnitude than the positive advective flux divergence, and the concentration tends to decrease. In the coastal region of Massachusetts Bay and Cape Cod Bay, because of the impact of the low concentration inflow from the Gulf of Maine at Cape Ann and the weak mortality, decline is the overall trend. In the Gulf of Maine, the tendency still varies with space, but in this period the leading trend is to decrease.

November-December to January-February

In this period, the growth in the coastal area of Cape Ann is comparable with that in the period from January-February to March-April and is the second strongest of all the six periods (secondary to that from March-April to May-June). The growth on Georges Bank is weaker than that in the coastal region of Cape Ann. The inflow at Cape Ann brings low-concentration water from the interior of the Gulf of Maine. The combined effect of the growth and the inflows enables the concentration in this coastal
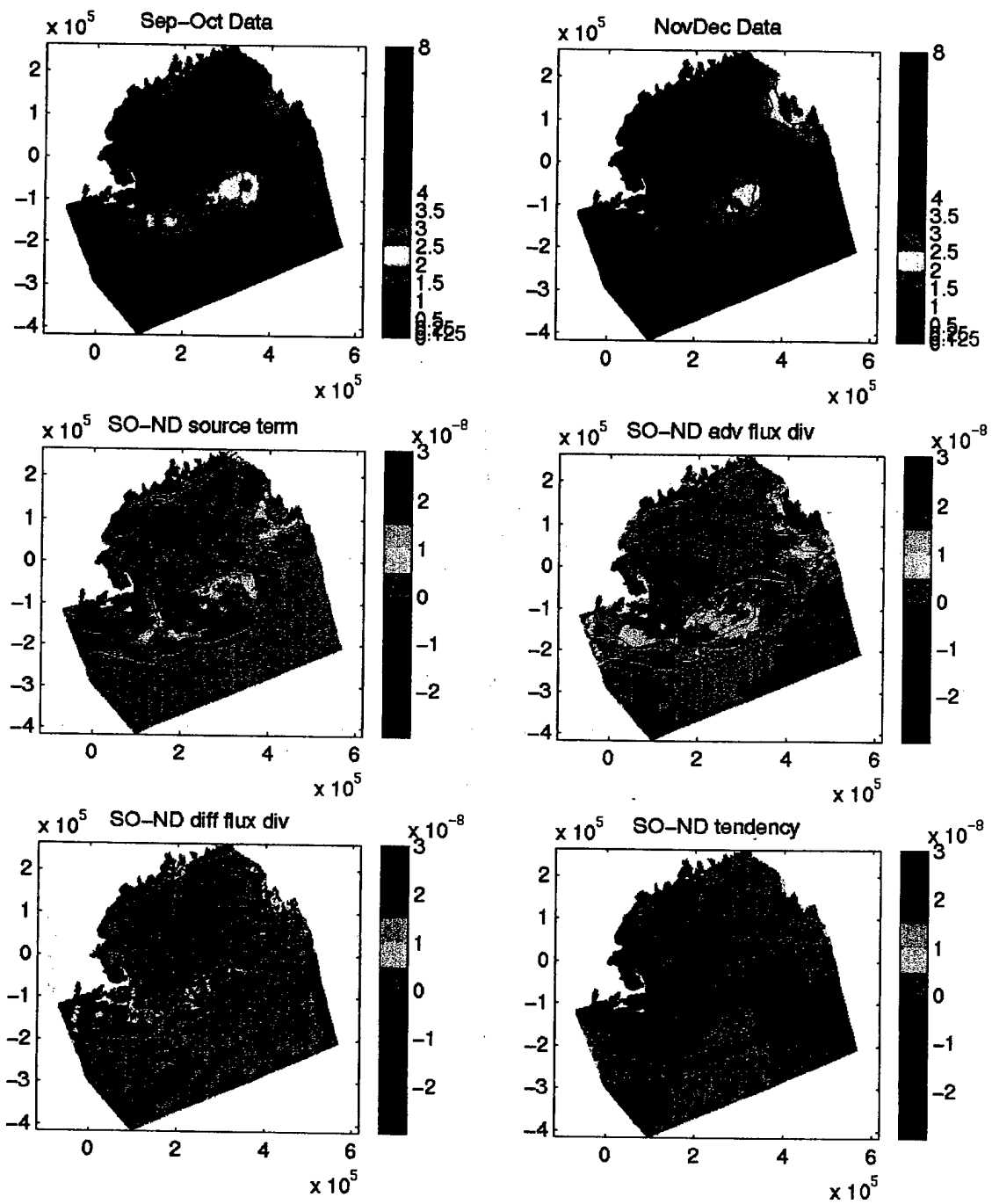
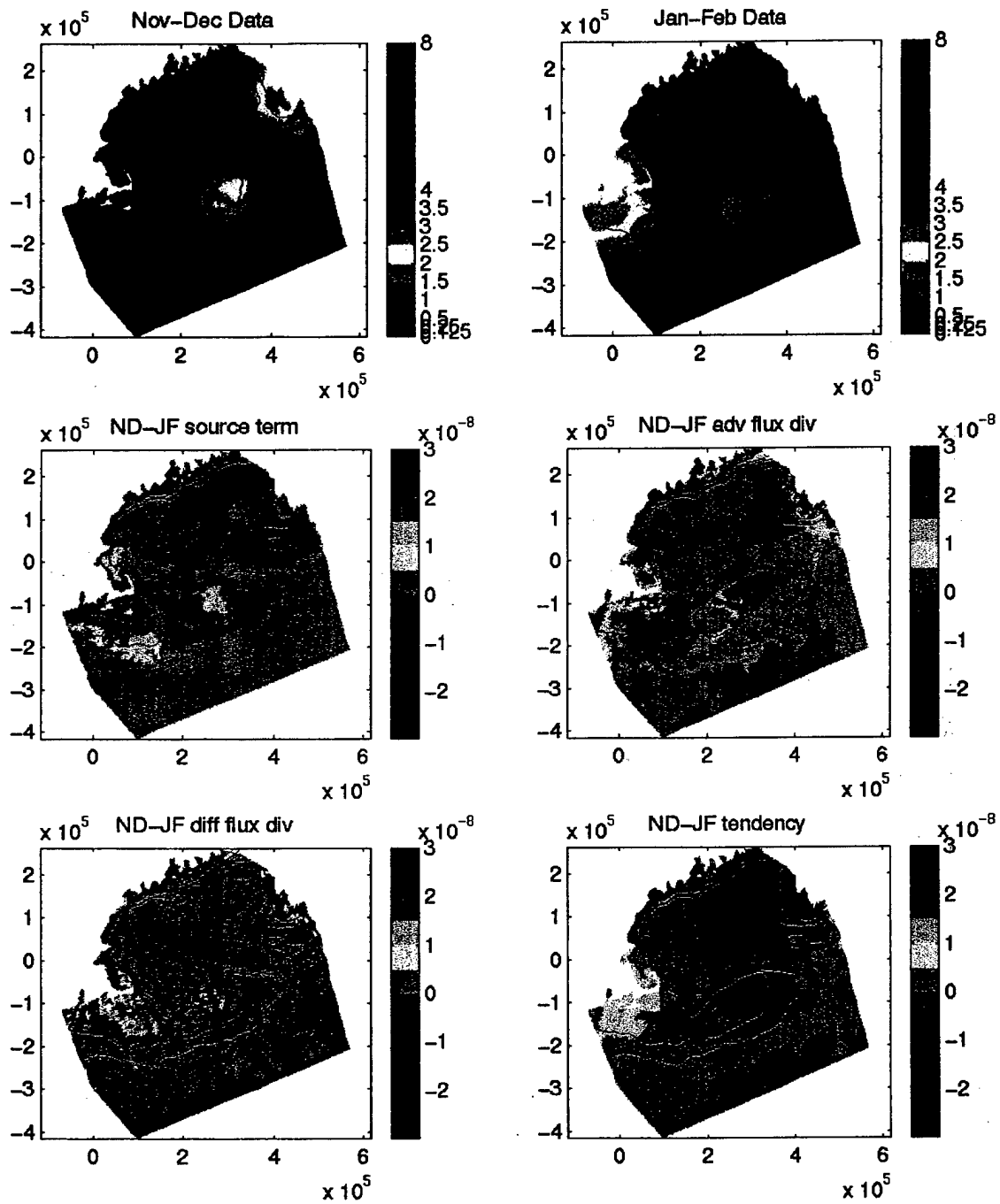Figure 4-8: The inversion results for the period from Sep-Oct to Nov-Dec.

Figure 4-9: The inversion results for the period from Nov-Dec to Jan-Feb.

region to increase, so as to accelerate the arrival of the spring bloom. On Georges Bank, with the declining seasonal stratification, the circulation on the Bank is less retentive than in the summer season. The negative advective flux divergence across the north flank overshadows the net growth. The positive advective flux divergence from the Bank crest to the Great South Channel has a smaller magnitude than the net mortality in most of the places where they intersect. Therefore, the concentration on Georges Bank decreases except over a limited area in the southwest, which is on the pathway of the outflow from the crest to the southwest. On the northeastern Bank, in a small region, the decreasing trend reaches its peak (i.e. the negative tendency has its maximum magnitude). The concentration in the western Gulf of Maine increases and that in the eastern Gulf of Maine decreases.

Diffusion does not have a systematic impact on the biology distribution, because the diffusive flux divergence term generally has a smaller magnitude than the source term and the advective flux divergence term. Sometimes it does have comparable magnitude, such as in the period from January-February to March-April on Georges Bank, but it is rather noisy and organized in small patches that do not affect the main features of the biology distribution. The only possible effect of diffusion is to smooth out the biology concentration.

4.3 Discussion

The results reveal significant seasonal and geographic variation of phytoplankton concentration, which is compatible with the climatological distribution patterns derived from the MARMAP data and the flow field. Two population centers are found in the Georges Bank-Gulf of Maine region, one is on Georges Bank itself and the other is in the western coastal region of the Gulf of Maine (i.e. the coastal region of Cape Ann,
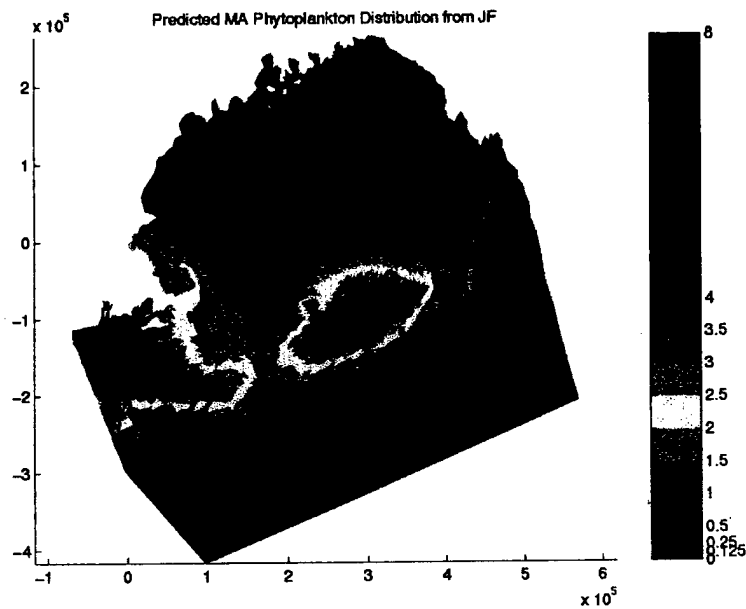
Figure 4-10: The predicted distribution of period Mar-Apr from period Jan-Feb.
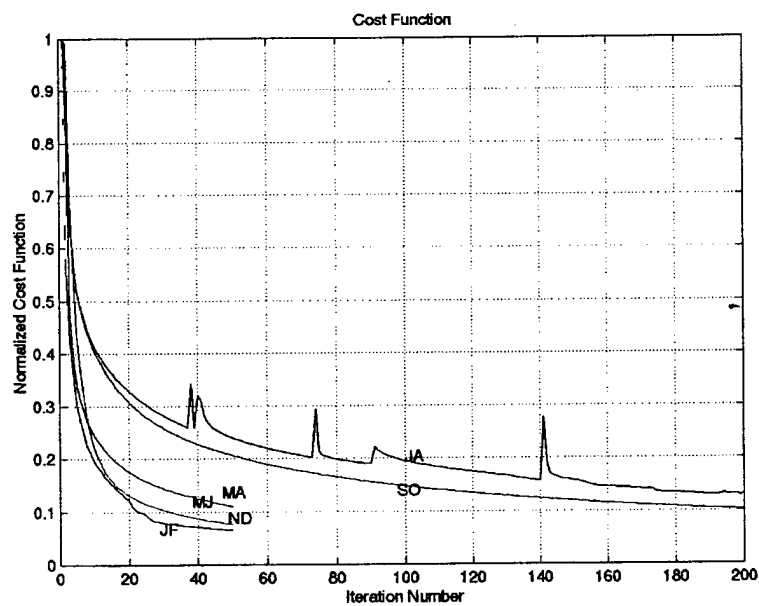

Figure 4-11: The cost function for each of the six assimilation experiments normalized to the initial value in each case.

Massachusetts Bay and Cape Cod Bay). During the period of January-February to March-April, it is a time of growth for both Georges Bank and the western coastal region of the Gulf of Maine and the growth is stronger on Georges Bank. Therefore, we define this period as a time of strong growth on Georges Bank and a time of moderate growth in the western coastal region of the Gulf of Maine. After the spring bloom peak in March-April, comes the time of decline from March-April to November-December. March-April to July-August is a period of faster decline, while from July-August until the end of the year, the concentration decreases slightly and is an interval of slight decline or relative stability. The changing trend from November-December to January-February on Georges Bank is opposite to that in the coastal region of the western Gulf of Maine. Phytoplankton abundance increases in the coastal region of the western Gulf of Maine and decreases on Georges Bank in the mean time. The decline on Georges Bank is even stronger than that during the period from July-August to November-December.

The most important and interesting results are that the seasonal cycles of the phytoplankton distribution are controlled by both the biological source and the physical advection which basically balances each other, and their relative significance varies with space and time. On Georges Bank, net growth (negative advective flux divergence) always lies north of the net mortality (positive advective flux divergence) and net growth (net mortality) mirrors negative advective flux divergence (positive advective flux divergence) in space. Net growth and net mortality thus respectively counterbalance negative and positive advective influence throughout the year despite the seasonal or spatial variability.

As we have shown in Chapter 2, the phytoplankton growth or mortality is very closely related to the availability of nutrients and sun light in the mixed layer. During winter, strong mixing continuously imports into the euphotic layer nutrients from below. While in summer, the stratification inhibits nutrient flux from below the

84

shallow mixed layer and so the nutrient supply is limited. Therefore, on Georges Bank, most of the biological growth occurs during the interval between January and April, when there is sufficient nutrients and light availability as well, while in other months the dominant source is weak growth or net mortality due to the lack of nutrients and/or light. In the coastal region of the western Gulf of Maine, the source term is positive throughout the year except from September-October to November-December. One possible reason is the availability of both nutrients and light resulting from the shallow depth and the consequent complete vertical mixing in this particular region.

The value of advective flux divergence is also a function of vertical mixing or stratification, especially on Georges Bank. During winter when there is deep mixing, the circulation pattern on Georges Bank is less retentive, and hence the distribution on the Bank is more susceptible to the influence of the flow from the Gulf of Maine than during summer when there is strong stratification. The advective flux divergence term (including both the advection from the Gulf of Maine on the north flank and the advection from the crest to the southwest) has the largest magnitude in the period of January-February to March-April. Its magnitude decreases with the arrival of summer. The spatial variation of the influence of advection on biology is quite notable, too. Generally speaking, the magnitude of the negative advective flux divergence from the Gulf of Maine is larger in magnitude on the north flank of Georges Bank than in the coastal region of the western Gulf of Maine. However, it is important to note that, advection is the controlling factor of tendency more often in the coastal region of the western Gulf than on the Bank, because of the small magnitude of the source term in the former region.

In the coastal region of the western Gulf of Maine, the tendency is generally controlled by the negative advective flux divergence, with the exception that from November-December to March-April, the contribution from advection is overshad-

owed by the moderately high net growth. The case on Georges Bank is quite different. The only time when the negative influence by the advection from the Gulf of Maine plays a controlling part together with the net mortality is the decline interval from March-April to May-June. During the season of increase from January-February to March-April, the advection from the Gulf of Maine is overshadowed by the positive source term. It is the net growth and the positive advection together that causes the increase of the phytoplankton concentration. From May-June to January-February, the decline trend is determined by the net mortality and also by the negative contribution from the Gulf of Maine. In this period, while the low concentration from the Gulf of Maine does help to overcome the net growth on the north flank, the major factor is the net mortality that overbalances the advection from the crest.

Chapter 5

Conclusions

In this thesis, we studied the interaction between physical and biological dynamics with two approaches. Firstly, in the Sargasso Sea, we looked into the response of a five-component ecosystem to the external forcing (heat flux, wind stress and surface salinity), investigating the sensitivity of the ecosystem to biochemical parameters. Secondly, in the Gulf of Maine-Georges Bank region, we explored the effect of the circulation field on the distribution of phytoplankton, and the relative importance of physical circulation and biological source to the concentration of phytoplankton as well.

In the research of the Sargasso Sea, the model results compare quite successfully with the observation and the model results of Doney et al., (1996). The default model results and the sensitivity experiments showed a seasonal cycle of physics and biology. In summer, the shallow seasonal thermocline depth and the weak convection inhibits the nutrients supply from below the mixed layer, therefore the concentrations of all the biochemical variables are low and limited to a shallow surface layer. In winter, the strong vertical convection and deep mixing make it possible for more nutrients to enrich the euphotic zone. Hence, right after the winter time, in March and April,

phytoplankton feeding upon nutrients reaches its spring bloom level. The bloom of zooplankton, which feeds on phytoplankton, follows that of phytoplankton with a time lag of about two weeks. The results of the sensitivity experiments show that zooplankton is usually more sensitive to the variation of biochemical parameters than phytoplankton. The system is sensitive to all the parameters except for the phytoplankton self-shading coefficient, ammonium half-saturation constant, photosynthesis efficiency parameter, and ammonium oxidation rate. For example, smaller detrital sinking rate and higher detrital renineralization rate provide higher nutrients concentration in the euphotic zone, while a smaller light extinction coefficient gives more and deeper solar radiation in the water column. Both circumstances allow the blooms to be more intense, deeper, and longer in time.

The research in the Gulf of Maine-Georges Bank region reveals seasonal and geographic variations of phytoplankton concentration, which are consistent with the MARMAP data. In this region, there are two population centers, one on the Georges Bank, and the other in the coastal region of the western Gulf of Maine. January-February to March-April shows a strong growth on Georges Bank and a medium growth in the coastal region of the western Gulf of Maine. March-April to July-August is the decline time for both of the two population centers. July-August to November-December shows a slight decline limited to relative stability period both on the Bank and in the coastal region of the western Gulf. November-December to January-February is a growth period in the coastal region of the western Gulf of Maine and a decline period on Georges Bank. The inversion results verify that the seasonal cycles of the phytoplankton distribution are controlled by both the biological source (net growth or mortality) and the physical advection by the circulation. Both the biological source and the physical advection are functions of space and time. The relative importance of them also varies with space and time. The seasonal cycles of the magnitude of net growth (mortality) approximately coincide with that of the

magnitude of the negative advection (positive advection), especially on Georges Bank. Therefore, net growth and net mortality basically counterbalance negative and positive advective flux divergences throughout the year, despite the seasonal or spatial variability. The magnitude of the negative advective flux divergence from the Gulf of Maine is larger on the north flank of Georges Bank than in the coastal region of the western Gulf of Maine. However, advection is the controlling factor of the tendency more often in the coastal region of the western Gulf of Maine than on Georges Bank, because of the small magnitude of the source term in the former region. This part of research also suggests that the two separated populations in the coastal area of the western Gulf of Maine and on Georges Bank are self-sustaining, and that Gulf of Maine is not the source for them.

In the two-dimensional model, the source term $R(x, y)$ is a function of space only, thus not representing the underlying biological processes realisticlly enough. A more realistic representation of the source term is needed. For the general topic of the interaction of biology and physics, a full three-dimensional biological-physical coupled model would undoubtedly provide better understanding and more realistic results. A major focus of future research is therefore to combine the above one-dimensional and two dimensional models used in this research, i.e. to build up a full three-dimensional biological-physical coupled model with a more sophisticated biological reaction term, and to investigate the response of the biological dynamics to the external forcing and the horizontal circulation.

Appendix A

Computation and mapping of the water column mean distribution of Chlorophyll a

Step1: Coordinate transformation.

Latitude and longitude coordinates of each station are transformed into map coordinates using a Fortran program written by Christopher E. Naimie of Dartmouth College (1996).

Step2: Select tile-averaged Chlorophyll a data for interpolation.

We first separate the data into the six two-month periods: Jan-Feb, Mar-Apr, May-Jun, Jul-Aug, Sep-Oct and Nov-Dec. For instance, in order to interpolate in the Jan-Feb period only the data measured in the first two-month period for all the years (1977-1988) are extracted.

Step3: Compute bathymetric gradient file.

Step4: Prepare the OAX grid files.

The estimation is centered in the middle of each two-month period with time scale

30 day and horizontal base scale 30 km. The horizontal correlation scales are specified in terms of the local cross-isobath and along-isobath directions which are defined by the bathymetric gradient vector.

Step5: Run OAX.

For our case the optimal estimation method "ESTIMATED MEAN" is used since it does not make the known zero mean assumption, unlike the "ANOMALY" method. The OAX model parameters including *global_scales* and *num_closest* are defined in a deck file. *Global_scales* are correlations used in determining the structure of the underlying data structure (Charles Hannah, 1995).

Step6: Extract level surface files.

In this step eleven files for depth levels 1 m, 5 m, 10 m, 15 m, 20 m, 25 m, 30 m, 35 m, 50 m, 75 m and 100 m are obtained.

Step7: Calculate the water column mean of Chlorophyll *a*.

We integrate Chlorophyll *a* over the upper 75 m of the water column and divide the integral by 75 m to get the mean. This two-month mean of the upper 75 m water column is called Chl_w.

Step8: Produce .s2r file with the Chl_w data.

The .s2r file is the FEM filetype, as detailed in the data file standards for the Gulf of Maine Project from the Numerical Methods Laboratory at Dartmouth College. This document is located in the OPNML notebook under External Documents. In the .s2r file there are two columns, the first of which is the node number and the second column is floating point.

Step9: Read and map the .s2r file.

Two matlab tools "read_s2r.m" and "colormesh2d.m" are used to read and plot the .s2r files. In order to facilitate comparison with the maps from the report of O'Reilly and Zetlin (1996), the colormaps we use are exactly the same as those O'Reilly and Zetlin used. The colormap for Chl_w is [0 0.125 0.25 0.5 1 2 4 8] μ/l.

Bibliography

[1] Beardsley, R.C., Butman, B., Geyer, W.R. and Smith, P. 1997. Physical oceanog-
raphy of the Gulf of Maine: an update. In: Proceeding of the Gulf of Maine
Ecosystem Dynamics Scientific Symposium and Workshop. Hanover NH. USA:
Regional Association for Research in the Gulf of Maine, Report 97-1, pp. 39-52.

[2] Bengtsson, L., M. Ghil and E. Kallen (Eds), 1981. Dynamic Meteorology: Data
Assimilation Methods. New York: Springer.

[3] Biglow, H.B. 1927. Physical oceanography of the Gulf of Maine. Bull. U.S. Bur.
Fish. 40:511-1027.

[4] Blumberg, A. F., and G. L. Mellor, 1987. A description of a three dimensional
coastal ocean circulation model, in Three-Dimensional Coastal Ocean Models,
Coastal Esturine Stud., vol. 4, edited by N. Heaps, pp. 1-16, AGU, Washington,
D. C.

[5] Bratseth, A. M. 1986. Statistical interpolation by means of successive corrections.
Tellus 38A, 439-447.

[6] Campbell, D. E. 1986. Process variability in the Gulf of Maine-a macroesturiane
environment. Esturian Variability, 261-275.

[7] Cohen, E. B. and M. D. Grosslein. 1987. Production on Georges Bank compared with other shelf ecosystems, in Georges Bank, R. H. Backus, ed., The MIT Press, Cambridge, MA, 383-391.

[8] Cohen, E. B., M. D. Grosslein, M. P. Sissenwine, F. Steimle and W. R. Wright, 1982. Energy budget of Georges Bank. Can. Spec. Pub. Fish. Aquat. Sci., 59, 95-107.

[9] Cressman, G. P. 1959. An operational objective analysis system. Mon. Wea. Rev. 87, 367-374.

[10] Derber, J. C. 1985. The variational four-dimensional assimilation of analyses using filtered models as constraints. PhD thesis, University of Wisconsin, Madson, Wisconcin.

[11] Dickey, T. D. 1991. The emergence of concurrenct high-resolution physical and bio-optical measurements in the upper ocean and their applications. Rev. Geophys. 29, 383-413.

[12] Le Dimet, F. X. and O. Talagrand. 1986. Variational algorithms for analysis and assimilation of meteorological observations: theoretical aspects. Tellus, Ser. A. 37, 309-322.

[13] Doney, S. C. D. M. Glover, and R. G. Najjar. 1996. A coupled, one-dimensional biological-physical model for the JGOFS Bermuda Atlantic Time Series Site, Deep Sea Res., Part I, in press.

[14] Eppley, R. W., Rogers, J. N. and J. McCarthy. 1969. Half-Saturation constant for uptake of Nitrate and Ammonium by Marine Phytoplankton. Limnology and Oceanography, Vol. 14, pp. 912-920.

[15] Esbensen S. K. and Y. Kushnir. 1981. The heat budget of the global ocean: an atlas based on estimates from surface marine observations. Climatic Research Institute, Report 29, Oregon State University, OR U. S. A.

[16] Fasham, M. J. R., H. W. Ducklow, and S. M. McKelvie. 1990. A nitrogen-based model of plankton dynamics in the oceanic mixed layer, J. Mar. Res., 48, 591-639.

[17] Gandin, L. S. 1963. Objective Analysis of Meteorlogical Fields. (From the Russian) Israel program for Scientific Translations, 1965, Jerusalem, 242 pp.

[18] Ghil, M. and P. Malanotte-Rizzoli. 1991. Data assimilation in meteorology and oceanography. Adv. Geophys. 33, 141-266.

[19] Ghil, P. E., W. Murray and M. H. Wright. 1981. Practical Optimization. Orlando: Academis Press.

[20] Green, P. J., and R. Sibson. 1978. Computing Dirichlet tessellations in the plane. Computer Journal 21: 168-173.

[21] Haidvogel, D. B. and A. R. Robinson (Eds). 1989. Special issue: data assimilation. Dyn. Atmos. Oceans 13, 171-513.

[22] Charles Hannah, Mary Jo Graca and John Loder. 1995. The OAX software package. http://aimsirl.bio.dfo.ca/channah/oax.demo.html.

[23] Horne, E. P. W., J. W. Loder, W. G. Harrison, R. Mohn, M. R. Lewis, B. Irwin and T. Platt. 1989. Nitrate supply and demand at the Georges Bank tidal front. Scient. Mar., 53, 145-158.

[24] George C. Hurtt and Robert A. Armstrong. 1996. A pelagic ecosystem model calibrated with BATS data. Deep-Sea Research II, Vol. 43, No. 2-3, pp. 653-683.

[25] Isemer H. and L. Hasse. 1985. The bunker climate atlas of the North Atlantic Ocean, Volume 2. Air-sea interactions. Springer-Verlag, New York, 252 pp.

[26] Jassby, A. D., and T. Platt. 1976. Mathematical formulation of the relationship between photosynthesis and light for phytopankton, Limnol. Oceanogr., 21, 540-547.

[27] Kalman, R. E. and R. S. Bucy. 1961. New results in linear filtering and prediction theory. J. Basic Engng (Transactions of the ASME) 83D, 95-108.

[28] Kalman, R. E. 1960. A new approach to linear filtering and prediction problems. J. Basic Engng (Transactions of the ASME) 82D, 35-45.

[29] Knap A. H., A. F. Michaels, R. L. Dow, R. J. Johnson, K. Gundersen, J. C. Sorensen, A. R. Close, M. Hammer, N. Bates, G. A. Knauer, S. E. Lohrenz, V. A. Asper, M. Thel, H. Duddow, H. Quinby. 1993. U.S. JGOFS Bermuda Atlantic Time-series Study, Data Report for BATS 25-BATS 36, October 1990-September 1991. U.S. JGOFS Planning Office. Woods Hole, MA, U.S.A., 339 pp.

[30] Knap A. H., A. F. Michaels, R. L. Dow, R. J. Johnson, K. Gundersen, J. C. Sorensen, A. R. Close, M. Hammer, G. A. Knauer, S. E. Lohrenz, V. A. Asper, M. Thel, H. Duddow, H. Quinby, P. Brewer and R. Bidigare. 1992. U.S. JGOFS Bermuda Atlantic Time-series Study, Data Report for BATS 13-BATS 24, October 1989-September 1990. U.S. JGOFS Planning Office. Woods Hole, MA, U.S.A., 345 pp.

[31] Knap A. H., A. F. Michaels, R. L. Dow, R. J. Johnson, K. Gundersen, G. A. Knauer, S. E. Lohrenz, V. A. Asper, M. Tuel, H. Duddow, H. Quinby and P. Brewer. 1991. U.S. JGOFS Bermuda Atlantic Time-series Study, Data Report for

BATS 1-BATS 12, October 1988-September 1989. U.S. JGOFS Planning Office. Woods Hole, MA, U.S.A., 286 pp.

[32] Lardner R. W. and S. K. Das. 1994. Optimal estimation of eddy viscosity for a quasi-three-dimensional numerical tidal and storm surge model. International Journal for Numerical Methods in Fluids, 18, 295-312.

[33] Lawson L. M., Y. H. Spitz, E. E. Hofmann and R. B. Long. 1995. A data assimilation technique applied to a predator-prey model, Bulletin of Mathematical Biology, 57, 593-617.

[34] Lewis, J. M. and J. C. Derber. 1985. The use of adjoint equations to solve a variational adjustment problem with adjective constraints. Tellus, Ser. A 37, 309-322.

[35] Lorenc, A. C. 1986. Analysis methods for numerical weather prediction. Q.J.R. met. Soc. 112, 1177-1194.

[36] Lorenc, A. C. 1988a. Optimal non-linear objective analysis. Q. J. R. met. Soc. 114, 205-240.

[37] Lorenc, A. C. 1988b. A practical approximation to optimal 4-dimemsional objective analysis. Mon. Wea. Rev. 116, 730-745.

[38] Lorenc, A. C. 1986. A global three-dimensional multivariate statistical interpolation scheme. Mon. Wea. Rev. 109, 701-721.

[39] Lynch, D.R., Holboke, M.J. and Naimie, C.E. 1997. The Maine coastal current: spring climatological circulation. Cont. Shelf Res. 18:607-639.

[40] Lynch, D.R., Ip, J.T.C., Naimie, C.E. and Werner, F.E. 1996. Comprehensive coastal circulation model with application to the Gulf of Maine. Cont. Shelf Res. 16:875-906.

[41] Mann, K.H. and Lazier, J.R.N. 1991. Dynamics of Marine Ecosystem (Biological-Physical interaction in the Oceans), Blackwell Scientific Publications, p.466.

[42] Margalef, R. 1967. Laboratory analogues of estuarine plankton systems, pp. 515-521. In: G. H. Lauff (ed.), Esturies. Amer. Assoc. Advan. Sci. Pub. No. 83. Washington, D. C.

[43] McGillicuddy, D.J., JR, Lynch, D.R., Moore, A.M., Gentleman, W.C., Davis, C.S., and Meise, C.J. 1998. Fisheries Oceanography. 7:3/4, 205-218.

[44] Mellor, G. L., User's Guide for a Three Dimensional, Primitive Equation Numerical Ocean Model, Prog. in Atmos. and Ocean Sci., 35 pp., Princeton Univ., Princeton, N. J., 1990.

[45] Mellor, G. L., and T. Yamada. 1982. Development of a turbulence closure model for geophysical fluid problems, Rev. Geophys., 20, 851-875.

[46] McClain C. R., W. E. Esaias, G. C. Feldman, J. Elrod, D. Endres, J. Fireston, M. Darzi, R. Evans and J. Brown. 1990. Physical and biological processes in the North Atlantic during the first GARP global experiment. Journal of Geophysical Research, 95, 18,027-18048.

[47] Menzel D. W and J. H. Ryther. 1960. The annual cycle of primary production in the Sargasso Sea off Bermuda. Deep-Sea Research, 6, 351-367.

[48] Mitchell B. G., E. A. Brody, O. Holm-Hansen, C. McClain and J. Bishop. 1991. Light limitation of phytoplankton biomass and macronutrient utilization. Limnology and Oceanography, 36, 16662-1677.

[49] Musgrave D. L., J. Chou and W. J. Jenkins. 1988. Application of a model of upper-ocean physics for studying seasonal cycles of oxygen, Journal of Geophysical Research, 93, 15,679-15,700.

[50] Naimie, C.E. 1996 Georges Bank residual circulation during weak and strong stratification periods: prognostic numerical model results. J. Geophys. Res. 101:6469-6486.

[51] Oguz, T., H. Ducklow, P. Malanotte-Rizzoli, S. Tugrul, N. Nezlin, U. Unluata. 1996. Simulation of plankton productivity cycle in the Black Sea by a one-dimensional physical-biological model, Journal of Geophysical Research. Vol. 101, No. C7, pp. 16,585-16,599.

[52] Panchang V. G. and J. J. O'Brien. 1989. On the determination of hydraulic model parameters using the adjoint state formulation. In: Modeling marine systems. A. M. Davis, editor, CRC Press, Boca Raton, Florida, pp. 6-18.

[53] O'Reilly, J. E. and Zetline, C. 1996. Monograph on the seasonal, horizontal, and vertical distribution of phytoplankton chlorophyll-a in the northeast U. S. continental shelf ecosystem. NOAA Technical Report, NMFS 139, 121 pp.

[54] O'Reilly, J. E., C. Evans-Zetlin and D. A. Busch. 1987. Primary production, in Georges Bank, R. H. Backus, ed., The MIT Press, Cambridge, MA, 220-233.

[55] Radach, G., and A. Moll. 1993. Estimation of the variability of production by simulating annual cycles of phytoplankton in the central North Sea, Prog. Oceanogr., 31,339-419.

[56] Riley, G. A. 1967a. Mathematical model of nutrient conditions in coastal waters. Bull. Bingham Oceanogr. Coll. 19:72-80.

[57] Riley, G. A. 1941. Plankton studies. IV. Georges Bank. Bull. Bingham Oveanogr. Coll. 7, 1-73.

[58] Ripley, B. D. 1981. Spatial Statistics. John Wiley and Sons. New York. 252 p.

[59] Sampson, R.J. 1988. SURFACE III Users Manual. Kansas Geological Survey, Lawrence, Kansas. Interactive Concepts Incorporated, Lawrence, KS. 277 p.

[60] Sharples, J., and P. Tett. 1994. Modelling the effect of physical variability on the midwater chlorophyll maximum, J. Mar. res., 52,219-238.

[61] Snyder J. P. 1987. Map Projections-A Working Manual. U.S. Geological Survey Professional Paper 1395. United States Government Printing Office, Washington, DC. 383 p.

[62] Uchupi, E., and J. A. Austin. 1987. Morphology. In: Georges Banks (R. H. Backus and D. W. Bourne, eds.). p. 25-30. MIT Press, Cambridge, MA.

[63] Uchupi, E. 1965. Map showing relarion of land and submarine topography, Nova Scotia to Florida. U.S.G.S. Miscellaneous Geological Investigations. Map I-451.

[64] Valiela, I. 1995. Marine Ecological Process, Springer Verlag ed., p. 686.

[65] Varela, R. A., A. Cruzado, J. Tintore, and E. G. Ladona. 1992. Modelling the deep-chlorophyll maximum: A coupled physical-biological approach, J. Mar. Res., 50, 441-463.

[66] Warren S. G., C. J. Halm, J. London, R. M. Chervin and R. L. Jenne.1988. Global distribution of total cloud and cloud type over the ocean. NCAR Technical Note, NCAR-TN 317.

[67] Woods Hole Oceanographic Institution and Bernuda Biological Station for Research. 1988. Station "S" off Bermuda, physical measurements 1954-1984. WHOI and BBSR Data Report, MA, U.S.A, 189 pp.

[68] Wroblewski J. S., J. L. Sarmiento and G. R. Flireal. 1988. An Ocean basin scale model of plankton dynamics in the North Atlantic 1. Solutions for the climatological oceanographic conditions in May. Global Biogeochemical Cycles, 2, 199-218.

[69] Wroblewski, J. 1977. A model of phytoplankton bloom formation during variable Oregon upwelling, J. Mar. Res., 35, 357-394.

[70] Zsoft. 1990. Technical reference Manual. Revision 4. Zsoft Corp. # p.